

## PHYSICS

## Pump-probe spectroscopy of chiral vibrational dynamics

Denis S. Tikhonov<sup>1,2†</sup>, Alexander Blech<sup>3†</sup>, Monika Leibscher<sup>3</sup>, Loren Greenman<sup>4</sup>, Melanie Schnell<sup>1,2\*</sup>, Christiane P. Koch<sup>3\*</sup>

A planar molecule may become chiral upon excitation of an out-of-plane vibration, changing its handedness during half a vibrational period. When exciting such a vibration in an ensemble of randomly oriented molecules with an infrared laser, half of the molecules will undergo the vibration phase-shifted by  $\pi$  compared to the other half, and no net chiral signal is observed. This symmetry can be broken by exciting the vibrational motion with a Raman transition in the presence of a static electric field. Subsequent ionization of the vibrating molecules by an extreme ultraviolet pulse probes the time-dependent net handedness via the photoelectron circular dichroism. Our proposal for pump-probe spectroscopy of molecular chirality, based on quantum-chemical theory and discussed for the example of the carbonyl chlorofluoride molecule, is feasible with current experimental technology.

## INTRODUCTION

Polyatomic molecules are often chiral, i.e., they exist in a left-handed and a right-handed version that cannot be superimposed by rotations and translations. The two conformers differ markedly in their chemical and biological behavior including a preference of handedness in amino acids and sugars in living organisms that is not yet understood (1). While handedness refers to the nuclear scaffold, molecular chirality is governed by the electronic structure of the molecule — left-handed molecules are separated from right-handed ones by a potential barrier. The height of this barrier determines the time scale over which the two conformers interconvert. Molecular chirality would be static only for infinitely high potential barriers. In real molecules, the lifetimes of a molecule as a specific enantiomer span a huge range (2). The barrier can be overcome by tunneling, vibrational excitation, or excitation to an achiral (and thus barrierless) electronically excited state. The corresponding interconversion dynamics may be exploited in asymmetric photochemistry (3). It is also at the core of proposals for coherent spectroscopies, for example, to measure the effect of parity violation (2, 4) or to coherently control enantiomeric purification (5, 6, 7).

None of these proposals has been realized in an experiment as of yet. This may be attributed to two main factors — (i) the complexity of the process involving chiral-to-achiral excitation, dynamics in the achiral state, and achiral-to-chiral deexcitation, all of which have to be driven selectively, and the choice of suitable molecules (8); and (ii) the lack of diagnostic tools for chirality-changing dynamics, in particular when the molecules are randomly oriented. The latter has been remedied by the advent of chiral vector observables that require only electric dipole transitions (9), and among these, photoelectron circular dichroism (PECD) (10–12) is particularly

versatile and suitable to monitor ultrafast dynamics (13–15). The complexity of studying interconversion dynamics can be reduced by separating the transitions between chiral and achiral states (15–17) and intermediate dynamics. However, fragmentation (16) and dissociation (15, 17) do not provide a viable route toward studying interconversion because the molecules are ripped apart. A more benign approach depositing less energy into the molecules is needed to probe interconversion dynamics, for example, using vibrational excitation.

Here, we suggest, based on state-of-the-art quantum-chemical calculations, to induce and probe chiral vibrational motion: achiral molecules have a symmetry plane in their equilibrium geometry but oscillate between left-handed and right-handed configurations during out-of-plane (OOP) vibrational motion (cf. Fig. 1). While the eigenstates are either symmetric or antisymmetric with respect to the symmetry plane and thus racemic, coherent superposition states are chiral (18–20) and change their handedness as a function of time. This can be probed, for example, with ultrafast

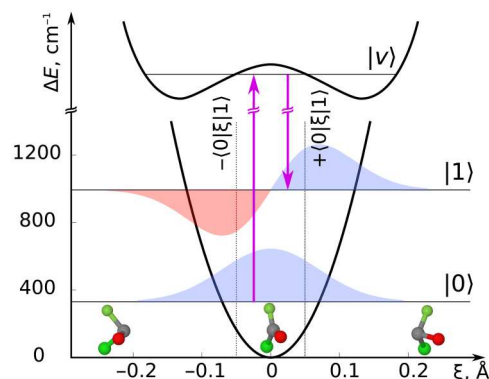


**Fig. 1. Creation of a chiral vibrational wave packet in a planar molecule.** Raman excitation (magenta arrows) of a superposition of the two lowest levels of the OOP vibration via a prochiral electronically excited state with vibrational level  $|\nu\rangle$ . In our example of carbonyl chlorofluoride (COFCl),  $\xi$  is the distance of the carbon atom from the O-F-Cl plane, and the vertical dotted lines at  $\pm \langle 0 | \xi | 1 \rangle$  indicate the maximal average displacement of the vibrational wave packet.

<sup>1</sup>Deutsches Elektronen-Synchrotron DESY, Notkestr. 85, 22607 Hamburg, Germany.

<sup>2</sup>Institute of Physical Chemistry, Christian-Albrechts-Universität zu Kiel, Max-Eyth-Str. 1, 24118 Kiel, Germany. <sup>3</sup>Dahlem Center for Complex Quantum Systems and Fachbereich Physik, Freie Universität Berlin, Arnimallee 14, 14195 Berlin, Germany.

<sup>4</sup>Department of Physics, Kansas State University, 116 Cardwell Hall, 1228 N. 17th St., Manhattan, KS 66506-2601, USA.

\*Corresponding author. Email: melanie.schnell@desy.de (M.S.); christiane.koch@fu-berlin.de (C.P.K.)

†These authors contributed equally to this work.

PECD (12–15). For a single molecule, the chirality is largest when probing at the maximal average OOP displacement, indicated by the vertical dotted lines in Fig. 1 for the simplest superposition involving only the ground and first excited level. However, for an ensemble of molecules with random orientations, the chirality will average out, yielding zero net enantiomeric excess. We show that Raman excitation in the presence of a static electric field yields a nonvanishing time-dependent enantiomeric excess, reflecting chiral vibrational motion in an ensemble of randomly oriented achiral molecules. We calculate the time-dependent PECD for the example of planar carbonyl chlorofluoride (COFCl) and discuss the requirements of a corresponding pump-probe study.

## RESULTS

Focusing on the simplest superposition,  $|\psi(t)\rangle = c_0|0\rangle + c_1e^{-i(E_1-E_0)t/\hbar}|1\rangle$ , the largest OOP displacement is obtained for equal weights. Assuming the molecule initially in its ground vibrational state, such a superposition can, in principle, be prepared by an infrared (IR) pulse or via ultraviolet (UV) Raman excitation. However, IR excitation does not produce a nonzero enantiomeric excess, as shown in the following. In both cases, the laser-molecule interaction depends on the orientation of the molecular axes relative to the laser polarization

$$\hat{H}_{\text{int}} = -\mathbf{E}(t) \mathcal{R}(\varphi, \theta, \chi) \hat{\boldsymbol{\mu}}$$

where  $\hat{\boldsymbol{\mu}}$  is the electric dipole moment in the molecular frame,  $\mathbf{E}(t)$  is the electric field in the laboratory frame, and  $\mathcal{R}$  is the rotation matrix connecting the two coordinate systems, dependent on the Euler angles  $\varphi$ ,  $\theta$ , and  $\chi$  (21).

The net enantiomeric excess  $\langle \langle \xi \rangle \rangle (t)$  in a gas-phase sample is obtained by averaging the mean OOP displacement,  $\langle \xi \rangle (t) = \langle \psi(t) | \xi | \psi(t) \rangle$ , over all molecular orientations (22). For an isotropic ensemble, the net enantiomeric excess is zero after rotational averaging for both IR and Raman excitation, because at least three mutually orthogonal fields are required to break the spatial symmetry (see section SI.B in the Supplementary Materials for a detailed explanation) (23). One option to fulfill this requirement is to apply a weak static electric field in conjunction with a circularly polarized Raman pulse. The direction of the relevant dipole moments, determined by the symmetry of the corresponding wave functions, is schematically shown in Fig. 2. In the presence of  $\mathbf{E}_{\text{static}}$  and assuming

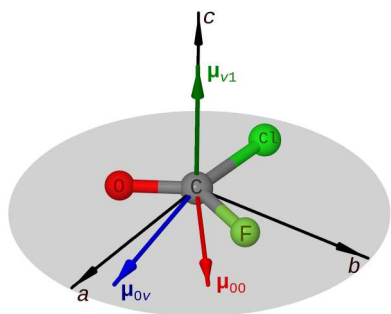


**Fig. 2. Molecular geometry together with the dipole moments relevant for creating a chiral vibrational wave packet.** Molecular frame representation of the permanent ( $\boldsymbol{\mu}_{00}$ ) and transition ( $\boldsymbol{\mu}_{0v}$  and  $\boldsymbol{\mu}_{v1}$ ) dipole moments of COFCl for a symmetric vibrational level  $|v\rangle$ .

the molecules to be in thermal (rotational) equilibrium at temperature  $T$ , the distribution of Euler angles is given by the Boltzmann factor  $p(\varphi, \theta, \chi) = \exp[\mathbf{E}_{\text{static}} \mathcal{R}(\varphi, \theta, \chi) \boldsymbol{\mu}_{00} / (k_B T)]$  with  $\boldsymbol{\mu}_{00} = \langle 0 | \hat{\boldsymbol{\mu}} | 0 \rangle$  the dipole moment of the molecule in the ground state, which lies in the molecular plane (see Fig. 2). Realistic field strengths are small on the scale of thermal excitations, and the Boltzmann factor can be approximated

$$p(\varphi, \theta, \chi) \approx 1 + \mathbf{E}_{\text{static}} \mathcal{R}(\varphi, \theta, \chi) \boldsymbol{\mu}_{00} / (k_B T) \quad (1)$$

We use perturbation theory (PT) in the following, which nicely captures the essence of the suggested excitation scheme. A Raman transition requires PT to second order and involves the transition dipole moments  $\boldsymbol{\mu}_{0v} = \langle 0 | \hat{\boldsymbol{\mu}} | v \rangle$  and  $\boldsymbol{\mu}_{v1} = \langle v | \hat{\boldsymbol{\mu}} | 1 \rangle$ , where  $v$  can be a symmetric or antisymmetric vibrational level in an electronically excited state (see Fig. 1). Averaging a second-order process over the rotational distribution Eq. 1 results in triple products of both electric fields and molecular dipole moments (see section SI.C in the Supplementary Materials),

$$\langle \langle \xi \rangle \rangle (t) \propto \langle 0 | \xi | 1 \rangle \sin(\omega_0 t) \frac{\tau^2}{T} \left[ 1 + \operatorname{erf} \left( \frac{t}{\tau} \right) \right]^2 \times [\mathbf{E}_{\text{static}} \cdot (\mathbf{E}_{L1} \times \mathbf{E}_{L2})] [\boldsymbol{\mu}_{00} \cdot (\boldsymbol{\mu}_{0v} \times \boldsymbol{\mu}_{v1})] \quad (2)$$

where we have assumed a circularly polarized Gaussian pulse with duration  $\tau$  and polarization directions  $\mathbf{E}_{L1/2}$ . Here,  $\omega_0$  denotes the OOP vibrational frequency, and the  $\operatorname{erf}(x)$  is the error function, which becomes approximately constant for  $t > 1.5\tau$ . As for many enantio-sensitive observables (9), this expression separates into products of the fields in the laboratory frame and molecular quantities in the molecular frame, which independently determine the amount of enantiomeric excess. The triple product of the fields is maximized by choosing all three fields orthogonal to each other, e.g., a static field along the  $z$  direction and a Raman pulse circularly polarized in the  $xy$  plane. If the intermediate state  $|v\rangle$  is totally symmetric ( $A'$ ), then only the molecular frame components  $\mu_{0v}^a$ ,  $\mu_{0v}^b$ , and  $\mu_{v1}^c$  can be nonzero, i.e.,  $\boldsymbol{\mu}_{0v}$  lies in the  $ab$  plane, and  $\boldsymbol{\mu}_{v1}$  is perpendicular to it (see Fig. 2). In general,  $\boldsymbol{\mu}_{0v}$  does not have the same direction as  $\boldsymbol{\mu}_{00}$ , and thus, the triple product  $[\boldsymbol{\mu}_{00} \cdot (\boldsymbol{\mu}_{0v} \times \boldsymbol{\mu}_{v1})]$  is nonzero. The same argument holds for antisymmetric ( $A''$ ) intermediate states, where the elements  $\mu_{0v}^c$ ,  $\mu_{v1}^a$ , and  $\mu_{v1}^b$  do not vanish by symmetry. Raman excitation in the presence of a weak static electric field can thus induce chiral wave packets with nonvanishing time-dependent enantiomeric excess in an ensemble of randomly oriented planar molecules. Excitation of the vibrational superposition with a circularly polarized IR pulse in the presence of a static electric field does not result in a net chiral signature. Within first-order PT, rotational averaging results in  $(\mathbf{E}_{\text{static}} \cdot \mathbf{E}_i)(\boldsymbol{\mu}_{00} \cdot \boldsymbol{\mu}_{01})$ , which vanishes because  $\boldsymbol{\mu}_{00}$  and  $\boldsymbol{\mu}_{01}$  are orthogonal because of molecular symmetry (details are found in section SI.D in the Supplementary Materials).

We now show that the nonvanishing time-dependent enantiomeric excess created by UV Raman excitation in the presence of a static field can be probed by a time-delayed ionizing pulse via PECD. PECD refers to the forward-backward asymmetry of photoelectron angular distributions (PADs) upon ionization of chiral molecules with left and right circularly polarized (LCP/RCP) light (10). Denoting the laboratory-frame photoelectron momentum by  $\mathbf{k}$  and following the convention in (24), it is given by the normalized

dichroic difference

$$\text{PECD}(\mathbf{k}) = \frac{\text{PAD}^{\text{LCP}}(\mathbf{k}) - \text{PAD}^{\text{RCP}}(\mathbf{k})}{[\text{PAD}^{\text{LCP}}(\mathbf{k}) + \text{PAD}^{\text{RCP}}(\mathbf{k})]/2} \quad (3)$$

For an achiral molecule, PECD is zero, while for a chiral molecule, PECD changes sign if one enantiomer is exchanged by the other. If a chiral wave packet is excited in an achiral molecule, then an oscillation of the PECD with the vibrational period is expected, provided that the probe pulse is sufficiently short.

The top panel of Fig. 3 displays PECD in a sample of COFCl molecules at a rotational temperature of 1 K as a function of the time delay  $t$  between the Raman excitation and the extreme ultraviolet (XUV) probe pulse. Velocity map images (VMIs) of PECD, i.e., the projection of Eq. 3 onto the  $yz$  plane, are shown for four time delays in the bottom panels of Fig. 3. The photoelectron asymmetry is presented in terms of the maximum dichroic difference along individual polar angles on the VMI detection plane, normalized

relative to the mean photoelectron intensity. Expressing PECD in terms of a single number by integrating over the forward and backward hemispheres as commonly done in experiments (25–27) is not possible here (see section SII.C in the Supplementary Materials). The pump pulse is assumed to be Gaussian with a peak intensity of  $10^{13}$  W/cm<sup>2</sup> and 150 fs full width at half maximum (FWHM), circularly polarized in the  $xy$  plane, and resonant to excited-state vibrational levels  $\nu = 20, 21$  (because PECD is a differential measurement, contributions from other transitions that might be driven by the Raman pulse cancel out). The probe pulse, with 5 fs FWHM and applied after a time delay  $t$ , is also circularly polarized in the  $xy$  plane. Its central frequency of 16.98 eV is chosen such that PECD is maximal. With these parameters, the energy dependence of the PAD is in good approximation given by the ionizing pulse spectrum (see section SII.C in the Supplementary Materials). The static electric field is taken along the  $z$  direction with a field strength of  $5 \times 10^5$  V/cm, which can be achieved, e.g., in modern Stark decelerators (28).

## DISCUSSION

The chiral pump-probe signal in Fig. 3 oscillates with a beat period of around 50 fs, as expected from the frequency of the OOP vibration. These oscillations confirm a net switch of handedness in the molecular ensemble on the time scale of the vibrational motion. Under the assumptions made above, the maximum PECD is of the order of 1.5%. This is an order of magnitude smaller than what has been observed in chiral molecules such as fenchone (12, 13) but is well within the capabilities of current photoelectron detection (27). The strength of PECD could be increased by optimizing the probe pulse, e.g., by using a polarization-shaped pulse (29, 30), which would maximize the asymmetry in the PAD. Alternatively, the chirality of the individual molecules could be increased by creating a vibrational superposition with larger maximal OOP displacement. While this has the chance to increase PECD, it may suffer from possible chiral zeros, because PECD can exhibit sign changes even if the handedness of the light and the molecule are kept fixed (31, 32). In addition, it comes at the expense of suitably tailoring the Raman excitation. A third option would be to amend the static electric field by an additional nonresonant laser pulse to increase the degree of orientation (33).

For the prediction of Fig. 3 to be observable, the coherent vibrational dynamics should not be washed out by decoherence. Mechanisms with time scales that are potentially of the order of 1 ps or below are rotational dephasing arising from rovibrational energy differences and intramolecular vibrational energy redistribution (IVR). A full account is provided in section SIII in the Supplementary Materials. We find the time scale for rotational dephasing to exceed 1 ps already at 70 K, becoming even larger for the cold ensembles that we consider. IVR is due to anharmonic coupling between different vibrational modes. Using ab initio molecular dynamics methods at the B3LYP-D3/def2-SVP level of theory, we find the relevant time scale to be  $\sim 3.5$  ps, comparable to what has been found for the C–O stretch mode in hexafluoroacetone (34) and sufficiently large for the coherent pump-probe spectroscopy that we suggest.

Other candidate molecules besides COFCl include formic acid, which has been used in enantioselective fragmentation (16) but comes with a somewhat shorter vibrational period of 32 fs, and

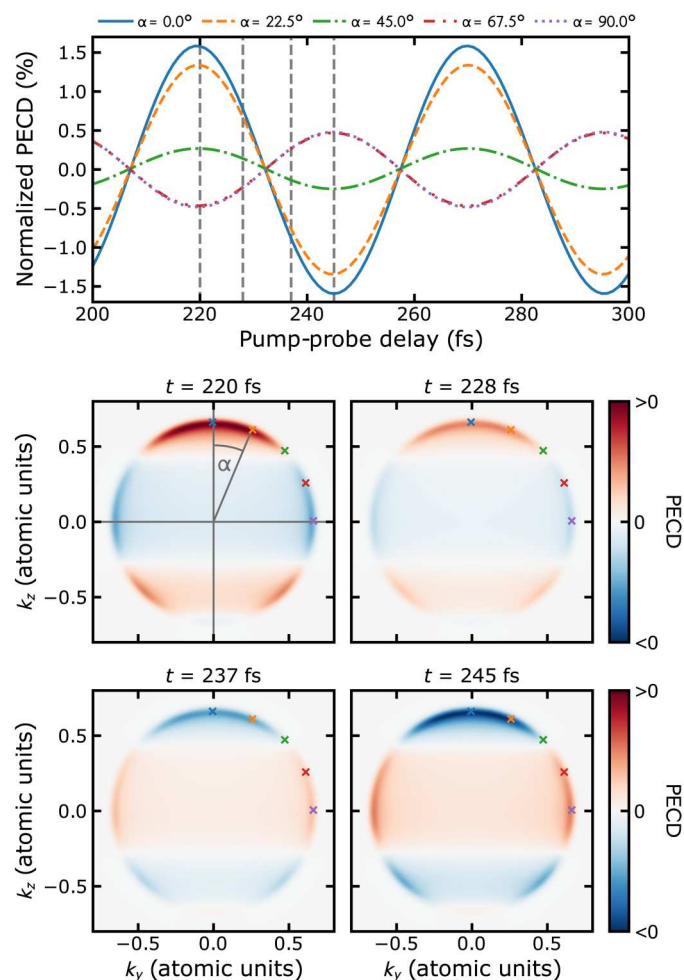


**Fig. 3. Pump-probe spectroscopy of light-induced chirality.** Maximum PECD signal at various polar angles normalized to the mean photoelectron intensity (top). Differential photoelectron spectra in the velocity map image (VMI)  $yz$  plane for the four times indicated by dashed vertical lines in the top panel. The crosses correspond to the polar angles shown in the top panel.



salts of the third main group such as  $\text{AlCl}_3$ . Substitution with two electron-withdrawing groups (halogens or  $\text{CF}_3$ ) and one electron-donating (like  $\text{CH}_3$ ) would make them more polar while keeping the boiling point low (35–37), important for use in molecular beams. The latter facilitate low vibrational and rotational temperatures, increasing the effective orientation in the static electric field and reducing rotational dephasing.

To summarize, we have laid out the principles for studying chiral vibrational dynamics in a gas-phase ensemble of planar, i.e., achiral molecules. Nonzero enantiomeric excess will be obtained if the field configuration, used to create the chiral vibrational superposition, ensures the characteristic triple products in rotational averages (9). Such a configuration can be realized with a static electric field, such that the molecules are uniaxially oriented, and an ultra-short circularly polarized Raman pulse that creates the vibrational wave packet, ideally with its polarization plane perpendicular to the static field. The induced time-dependent chirality can be probed by PECD upon ionization with a sufficiently short, time-delayed, circularly polarized pulse. The chiral signals that we predict on the basis of quantum-chemical calculations for the test case of planar COFCl are readily observable, and a corresponding experiment is feasible with existing technical capabilities. Such studies of time-dependent chirality, following the change of handedness in the course of vibrational motion, would provide a stepping stone to lastly realize long-standing proposals for chiral molecules, including the measurement of parity violation (2, 4) and enantiomeric purification with light (5–7).

## METHODS

The electronic properties of the neutral molecule, i.e., potentials and dipole moments as a function of the OOP mode  $\xi$ , are calculated at the B3LYP level of theory (38–41) with the cc-pVTZ basis set (42), making use of the Tamm-Dancoff approximation (43) for the excited state, using Orca 4 (44). The vibrational eigenstates and (transition) dipole moments  $\mu_{00}$ ,  $\mu_{0v}$ , and  $\mu_{v1}$  are obtained by numerically solving the vibrational Schrödinger equation using a discrete variable representation (45) for the ground and excited electronic state. The vibrational frequency of the electronic ground-state OOP mode and the UV absorption spectrum reproduce the available experimental data for COFCl (see section SII, A and B, in the Supplementary Materials for details) (46–50).

To describe ionization, the transition dipole moments for the bound-continuum transition are needed. The bound-state orbitals of COFCl required to this end have been calculated within the Hartree-Fock approximation using MOLPRO (51, 52) with the aug-cc-pVTZ basis set (53) for a set of molecular configurations along the OOP coordinate. The continuum wave functions and ionization matrix elements have been obtained with ePolyScat (54, 55) in the frozen-core static-exchange approximation following (29, 30, 56). Ionization is assumed to be instantaneous, keeping the molecular configuration fixed at its equilibrium structure except for the OOP vibration. The instantaneous PAD of the vibrating molecule is then obtained by averaging the ionization matrix elements over the OOP coordinate. The interaction with both pump and probe pulse is treated perturbatively, which is justified because by very small transition moments. PADs are calculated for different Euler angles and then averaged over the rotational distribution (1) (see also section SII.C in the Supplementary Materials).

The IVR lifetime was estimated using quantum-chemical molecular dynamics simulations done with Orca 4 (44) at the B3LYP-D3BJ/def2-SVP (38–41, 57, 58) level of theory. The initial coordinates of the nuclei were taken as displacements along the OOP coordinate  $\xi$  with all other modes in their equilibrium geometry, while the velocities were assigned using a Maxwell-Boltzmann distribution at a temperature of 300 K. More details are available in section SIII.C in the Supplementary Materials.

## Supplementary Materials

This PDF file includes:

Sections I to VI  
Figs. S1 to S11  
Tables S1 to S4  
References

## REFERENCES AND NOTES

- D. P. Glavin, A. S. Burton, J. E. Elsil, J. C. Aponte, J. P. Dworkin, The search for chiral asymmetry as a potential biosignature in our solar system. *Chem. Rev.* **120**, 4660–4689 (2020).
- M. Quack, J. Stohner, M. Willeke, High-resolution spectroscopic studies and theory of parity violation in chiral molecules. *Annu. Rev. Phys. Chem.* **59**, 741–769 (2008).
- U. Raucci, H. Weir, C. Bannwarth, D. M. Sanchez, T. J. Martinez, Chiral photochemistry of achiral molecules. *Nat. Commun.* **13**, 2091 (2022).
- C. Fábri, L. Horný, M. Quack, Tunneling and parity violation in trisulfane (HSSSH): An almost ideal molecule for detecting parity violation in chiral molecules. *ChemPhysChem* **16**, 3584–3589 (2015).
- Y. Fujimura, L. González, K. Hoki, J. Manz, Y. Ohtsuki, Selective preparation of enantiomers by laser pulses: Quantum model simulation for  $\text{H}_2\text{POSH}$ . *Chem. Phys. Lett.* **306**, 1–8 (1999).
- D. Gerbasi, P. Brumer, I. Thanopoulos, P. Král, M. Shapiro, Theory of the two step enantiomeric purification of 1,3 dimethylallene. *J. Chem. Phys.* **120**, 11557–11563 (2004).
- E. F. Thomas, N. E. Henriksen, Phase-modulated nonresonant laser pulses can selectively convert enantiomers in a racemic mixture. *J. Phys. Chem. Lett.* **8**, 2212–2219 (2017).
- M. Quack, G. Seyfang, G. Wichmann, Fundamental and approximate symmetries, parity violation and tunneling in chiral and achiral molecules. *Adv. Quantum Chem.* **81**, 51–104 (2020).
- A. F. Ordonez, O. Smirnova, Generalized perspective on chiral measurements without magnetic interactions. *Phys. Rev. A* **98**, 063428 (2018).
- B. Ritchie, Theory of the angular distribution of photoelectrons ejected from optically active molecules and molecular negative ions. *Phys. Rev. A* **13**, 1411–1415 (1976).
- N. Böwering, T. Lischke, B. Schmidtke, N. Müller, T. Khalil, U. Heinzmann, Asymmetry in photoelectron emission from chiral molecules induced by circularly polarized light. *Phys. Rev. Lett.* **86**, 1187–1190 (2001).
- C. Lux, M. Wollenhaupt, T. Bolze, Q. Liang, J. Köhler, C. Sarpe, T. Baumert, Circular dichroism in the photoelectron angular distributions of camphor and fenchone from multiphoton ionization with femtosecond laser pulses. *Angew. Chem. Int. Ed.* **51**, 5001–5005 (2012).
- A. Comby, S. Beaulieu, M. Boggio-Pasqua, D. Descamps, F. Légaré, L. Nahon, S. Petit, B. Pons, B. Fabre, Y. Mairesse, V. Blanchet, Relaxation dynamics in photoexcited chiral molecules studied by time-resolved photoelectron circular dichroism: Toward chiral femtochemistry. *J. Phys. Chem. Lett.* **7**, 4514–4519 (2016).
- S. Beaulieu, A. Comby, A. Clergerie, J. Caillat, D. Descamps, N. Dudovich, B. Fabre, R. Géraux, F. Légaré, S. Petit, B. Pons, G. Porat, T. Ruchon, R. Taïeb, V. Blanchet, Y. Mairesse, Attosecond-resolved photoionization of chiral molecules. *Science* **358**, 1288–1294 (2017).
- V. Svoboda, N. B. Ram, D. Baykusheva, D. Zindel, M. D. J. Waters, B. Spenger, M. Ochsner, H. Herburger, J. Stohner, H. J. Wörner, Femtosecond photoelectron circular dichroism of chemical reactions. arXiv:2206.04099 [physics.chem-ph] (8 June 2022).
- K. Fehre, S. Eckart, M. Kunitski, M. Pitzer, S. Zeller, C. Janke, D. Trabert, J. Rist, M. Weller, A. Hartung, L. P. H. Schmidt, T. Jahnke, R. Berger, R. Dörner, M. S. Schöffler, Enantioselective fragmentation of an achiral molecule in a strong laser field. *Sci. Adv.* **5**, eaau7923 (2019).
- D. Baykusheva, D. Zindel, V. Svoboda, E. Bommeli, M. Ochsner, A. Tehlar, H. J. Wörner, Real-time probing of chirality during a chemical reaction. *Proc. Natl. Acad. Sci. U.S.A.* **116**, 23923–23929 (2019).

18. S. S. Bychkov, B. A. Grishanin, V. N. Zadkov, H. Takahashi, Laser coherent control of molecular chiral states via entanglement of the rotational and torsional degrees of freedom. *J. Raman Spectrosc.* **33**, 962–973 (2002).
19. D. V. Zhdanov, V. N. Zadkov, Coherent control of chirality in ensemble of randomly oriented molecules using a sequence of short laser pulses. *Laser Physics* **20**, 107–118 (2010).
20. A. F. Ordóñez, O. Smirnova, Propensity rules in photoelectron circular dichroism in chiral molecules. I. Chiral hydrogen. *Phys. Rev. A* **99**, 043416 (2019).
21. C. P. Koch, M. Lemeshko, D. Sugny, Quantum control of molecular rotation. *Rev. Mod. Phys.* **91**, 035005 (2019).
22. D. L. Andrews, T. Thirunamachandran, On three-dimensional rotational averages. *J. Chem. Phys.* **67**, 5026–5033 (1977).
23. M. Leibscher, T. F. Giesen, C. P. Koch, Principles of enantio-selective excitation in three-wave mixing spectroscopy of chiral molecules. *J. Chem. Phys.* **151**, 014302 (2019).
24. I. Powis, in *Photoelectron Circular Dichroism in Chiral Molecules*, S. A. Rice, Ed. (John Wiley & Sons Ltd., 2008), chap. 5, pp. 267–329.
25. M. H. M. Janssen, I. Powis, Detecting chirality in molecules by imaging photoelectron circular dichroism. *Phys. Chem. Chem. Phys.* **16**, 856–871 (2014).
26. C. Lux, M. Wollenhaupt, C. Sarpe, T. Baumert, Photoelectron circular dichroism of bicyclic ketones from multiphoton ionization with femtosecond laser pulses. *ChemPhysChem* **16**, 115–137 (2015).
27. A. Kastner, C. Lux, T. Ring, S. Züllighoven, C. Sarpe, A. Senftleben, T. Baumert, Enantiomeric excess sensitivity to below one percent by using femtosecond photoelectron circular dichroism. *ChemPhysChem* **17**, 1119–1122 (2016).
28. G. Meijer, in *Molecular Beams in Physics and Chemistry: From Otto Stern's Pioneering Exploits to Present-Day Feats*, B. Friedrich, H. Schmidt-Böcking, Eds. (Springer International Publishing, 2021), pp. 463–476.
29. R. E. Goetz, C. P. Koch, L. Greenman, Quantum control of photoelectron circular dichroism. *Phys. Rev. Lett.* **122**, 013204 (2019).
30. R. E. Goetz, C. P. Koch, L. Greenman, Perfect control of photoelectron anisotropy for randomly oriented ensembles of molecules by XUV REMPI and polarization shaping. *J. Chem. Phys.* **151**, 074106 (2019).
31. E. Ruch, Chiral derivatives of achiral molecules: Standard classes and the problem of a right-left classification. *Angew. Chem. Int. Ed.* **16**, 65–72 (1977).
32. G. Hartmann, M. Ilchen, P. Schmidt, C. Küstner-Wetekam, C. Ozga, F. Scholz, J. Buck, F. Trinter, J. Viefhaus, A. Ehresmann, M. S. Schöffler, A. Knie, P. V. Demekhin, Recovery of high-energy photoelectron circular dichroism through fano interference. *Phys. Rev. Lett.* **123**, 043202 (2019).
33. B. Friedrich, D. Herschbach, Enhanced orientation of polar molecules by combined electrostatic and nonresonant induced dipole forces. *J. Chem. Phys.* **111**, 6157–6160 (1999).
34. S. V. Krasnoshechekov, V. B. Laptev, S. A. Klimin, I. K. Gainullin, A. A. Makarov, Overtone spectroscopy of  $\nu(\text{C}=\text{O})$  stretching vibration of hexafluoroacetone: Experimental and ab initio determination of peak positions, absolute intensities, and band shapes. *Spectrochim. Acta A Mol. Biomol. Spectrosc.* **238**, 118396 (2020).
35. S. Takeda, R. Terao, The infrared spectra of alkylaluminum-ether complexes. *Bull. Chem. Soc. Jpn.* **38**, 1567–1574 (1965).
36. H. Hoberg, S. Krause, The Al—Al bond as a readily accessible structural unit in organometallic compounds. *Angew. Chem. Int. Ed.* **15**, 694–694 (1976).
37. A. Kunicki, W. Kosińska, M. Bolesławski, S. Pasykiewicz, The  $^1\text{H}$  NMR spectra of methylmethoxyaluminum chloride and methylmethoxyaluminum iodide. *J. Organomet. Chem.* **141**, 283–288 (1977).
38. A. D. Becke, Density-functional thermochemistry. III. The role of exact exchange. *J. Chem. Phys.* **98**, 5648–5652 (1993).
39. C. Lee, W. Yang, R. G. Parr, Development of the Colle-Salvetti correlation-energy formula into a functional of the electron density. *Phys. Rev. B* **37**, 785–789 (1988).
40. S. H. Vosko, L. Wilk, M. Nusair, Accurate spin-dependent electron liquid correlation energies for local spin density calculations: A critical analysis. *Can. J. Phys.* **59**, 1200–1211 (1980).
41. P. J. Stephens, F. J. Devlin, C. F. Chabalowski, M. J. Frisch, Ab initio calculation of vibrational absorption and circular dichroism spectra using density functional force fields. *J. Phys. Chem.* **98**, 11623–11627 (1994).
42. T. H. Dunning Jr., Gaussian basis sets for use in correlated molecular calculations. i. The atoms boron through neon and hydrogen. *J. Chem. Phys.* **90**, 1007–1023 (1989).
43. S. Hirata, M. Head-Gordon, Time-dependent density functional theory within the Tamm-Dancoff approximation. *Chem. Phys. Lett.* **314**, 291–299 (1999).
44. F. Neese, The ORCA program system. *Wiley Interdiscip. Rev. Comput. Mol. Sci.* **2**, 73–78 (2012).
45. D. T. Colbert, W. H. Miller, A novel discrete variable representation for quantum mechanical reactive scattering via the S-matrix Kohn method. *J. Chem. Phys.* **96**, 1982–1991 (1992).
46. I. Zanon, G. Giacometti, D. Piccio, The electronic spectrum of FCICO. *Spectrochim. Acta A Mol. Biomol. Spectrosc.* **19**, 301–3E7 (1963).
47. N. Heineking, W. Jager, M. Gerry, Isotopic and vibrational satellites in the rotational spectrum of carbonyl chloride fluoride. *J. Mol. Spectrosc.* **158**, 69–81 (1993).
48. C. Maul, C. Dietrich, T. Haas, K.-H. Gericke, Photodissociation dynamics of carbonyl chloride fluoride and its implications for phosgene three body decay. *Phys. Chem. Chem. Phys.* **1**, 1441–1446 (1999).
49. A. Perrin, J. Demaison, G. Toon, The  $\nu_1$ ,  $\nu_2$ , and  $\nu_3$  bands of carbonyl chlorofluoride (COFCl) at 5.3, 9.1, and 13.1  $\mu\text{m}$ : Position and intensity parameters and their use for atmospheric studies. *J. Quant. Spectrosc. Radiat. Transf.* **112**, 1266–1279 (2011).
50. H. Keller-Rudek, G. K. Moortgat, R. Sander, R. Sörensen, The MPI-Mainz UV/VIS spectral atlas of gaseous molecules of atmospheric interest. *Earth Syst. Sci. Data* **5**, 365–373 (2013).
51. H.-J. Werner, P. J. Knowles, G. Knizia, F. R. Manby, M. Schütz, P. Celani, T. Korona, R. Lindh, A. Mitrushenkov, G. Rauhut, K. R. Shamasundar, T. B. Adler, R. D. Amos, A. Bernhardsson, A. Berning, D. L. Cooper, M. J. O. Deegan, A. J. Dobbyn, F. Eckert, E. Goll, C. H. I. A. Hesselmann, G. Hetzer, T. Hrenar, G. Jansen, C. Köppl, Y. Liu, A. W. Lloyd, R. A. Mata, A. J. May, S. J. McNicholas, W. Meyer, M. E. Mura, A. Nicklass, D. P. O'Neill, P. Palmieri, D. Peng, K. Pflüger, R. Pitzer, M. Reiher, T. Shiozaki, H. Stoll, A. J. Stone, R. Tarroni, T. Thorsteinsson, M. Wang, MOLPRO, version 2012.1, a package of ab initio programs.
52. H.-J. Werner, P. J. Knowles, G. Knizia, F. R. Manby, M. Schütz, Molpro: A general-purpose quantum chemistry program package. *Wiley Interdiscip. Rev. Comput. Mol. Sci.* **2**, 242–253 (2012).
53. R. A. Kendall, T. H. Dunning Jr., R. J. Harrison, Electron affinities of the first-row atoms revisited. Systematic basis sets and wave functions. *J. Comp. Phys.* **96**, 6796–6806 (1992).
54. F. A. Gianturco, R. R. Lucchese, N. Sanna, Calculation of low-energy elastic cross sections for electron- $\text{CF}_4$  scattering. *J. Chem. Phys.* **100**, 6464–6471 (1994).
55. A. P. P. Natalense, R. R. Lucchese, Cross section and asymmetry parameter calculation for sulfur 1s photoionization of SF<sub>6</sub>. *J. Chem. Phys.* **111**, 5344–5348 (1999).
56. P. Hockett, M. Wollenhaupt, C. Lux, T. Baumert, Complete photoionization experiments via ultrafast coherent control with polarization multiplexing. II. Numerics and analysis methodologies. *Phys. Rev. A* **92**, 013411 (2015).
57. S. Grimme, S. Ehrlich, L. Goerigk, Effect of the damping function in dispersion corrected density functional theory. *J. Comput. Chem.* **32**, 1456–1465 (2011).
58. F. Weigend, R. Ahlrichs, Balanced basis sets of split valence, triple zeta valence and quadruple zeta valence quality for h to rn: Design and assessment of accuracy. *Phys. Chem. Chem. Phys.* **7**, 3297–3305 (2005).
59. P. Atkins, J. Paula, *Atkins' Physical Chemistry* (Oxford Univ. Press, 2008).
60. M. Mantina, A. C. Chamberlin, R. Valero, C. J. Cramer, D. G. Truhlar, Consistent van der Waals radii for the whole main group. *Chem. A Eur. J.* **113**, 5806–5812 (2009).

**Acknowledgments:** Computations in this research were enabled, in part, by the Beocat Research Cluster at Kansas State University and the Maxwell Computational Resources operated at Deutsches Elektronen-Synchrotron DESY, Hamburg, Germany. **Funding:** This work has been funded by the Deutsche Forschungsgemeinschaft (DFG, German Research Foundation) project number 328961117 - SFB 1319 ELCH. L.G. acknowledges support from the U.S. Department of Energy, Office of Science, Basic Energy Sciences, under award no. DE-FG02-86ER13491. **Author contributions:** D.S.T. conceived the creation of a chiral wave packet and carried out the quantum chemical calculations for the bound states of COFCl. A.B., D.S.T., and M.L. worked out the conditions for a nonzero chiral signal in a gas-phase sample of molecules. A.B. carried out the calculations of PECED, with help from L.G. M.S. and C.P.K. supervised the work. All authors analyzed and discussed the results and contributed to the writing of the manuscript. **Competing interests:** The authors declare that they have no competing interests. **Data and materials availability:** All data needed to evaluate the conclusions in the paper are present in the paper and/or the Supplementary Materials.

Submitted 20 July 2022  
Accepted 25 October 2022  
Published 7 December 2022  
10.1126/sciadv.ade0311

## Pump-probe spectroscopy of chiral vibrational dynamics

Denis S. TikhonovAlexander BlechMonika LeibscherLoren GreenmanMelanie SchnellChristiane P. Koch

*Sci. Adv.*, 8 (49), eade0311. • DOI: 10.1126/sciadv.ade0311

### View the article online

<https://www.science.org/doi/10.1126/sciadv.ade0311>

### Permissions

<https://www.science.org/help/reprints-and-permissions>

Use of this article is subject to the [Terms of service](#)

---

*Science Advances* (ISSN ) is published by the American Association for the Advancement of Science. 1200 New York Avenue NW, Washington, DC 20005. The title *Science Advances* is a registered trademark of AAAS. Copyright © 2022 The Authors, some rights reserved; exclusive licensee American Association for the Advancement of Science. No claim to original U.S. Government Works. Distributed under a Creative Commons Attribution License 4.0 (CC BY).

Supplementary Materials for  
**Pump-probe spectroscopy of chiral vibrational dynamics**

Denis S. Tikhonov *et al.*

Corresponding author: Melanie Schnell, [melanie.schnell@desy.de](mailto:melanie.schnell@desy.de);  
Christiane P. Koch, [christiane.koch@fu-berlin.de](mailto:christiane.koch@fu-berlin.de)

*Sci. Adv.* **8**, eade0311 (2022)  
DOI: 10.1126/sciadv.ade0311

**This PDF file includes:**

Sections SI to SVI  
Figs. S1 to S11  
Tables S1 to S4  
References

## I. GENERAL CONSIDERATIONS

### A. Geometry of the envisioned experiment

The proposed experiment is sketched in Figure S1: Two oppositely charged electrodes (indicated by the red and green rings with "+" and "-" for the charges) create a static electric field with strength  $\mathbf{E}_{\text{static}}$ . A circularly polarized UV pulse, for example the 4th harmonic of a Ti:Sa laser, is sent to a sample of planar molecules such that its polarization, specified by the two orthogonal electric fields  $\mathbf{E}_{L1}$  and  $\mathbf{E}_{L2}$ , is orthogonal to the static electric field. Hence the triple product  $\mathbf{E}_{\text{static}} \cdot [\mathbf{E}_{L1} \times \mathbf{E}_{L2}] \neq 0$ . The electric field tends to orient the molecules by their permanent dipole moment  $\mu_{00}$ , while the UV pump pulse creates a coherent chiral vibrational wavepacket by resonant Raman excitation of the out-of-plane vibration. The resulting time-dependent chirality can be probed by a circularly polarized XUV probe pulse with the same propagation direction as the UV pump pulse. The probe ionizes the molecular ensemble, and photoelectron angular distributions (PAD) are measured using velocity map imaging (VMI). Recording PADs with both helicities of the probe pulse and taking their difference allows for quantifying the produced enantiomeric excess in terms of photoelectron circular dichroism (PECD). Figure S1 shows one possible configuration that would allow to use the static electric field of the VMI for  $\mathbf{E}_{\text{static}}$ . Other field configurations might exist that are more suitable for a given experimental setup.

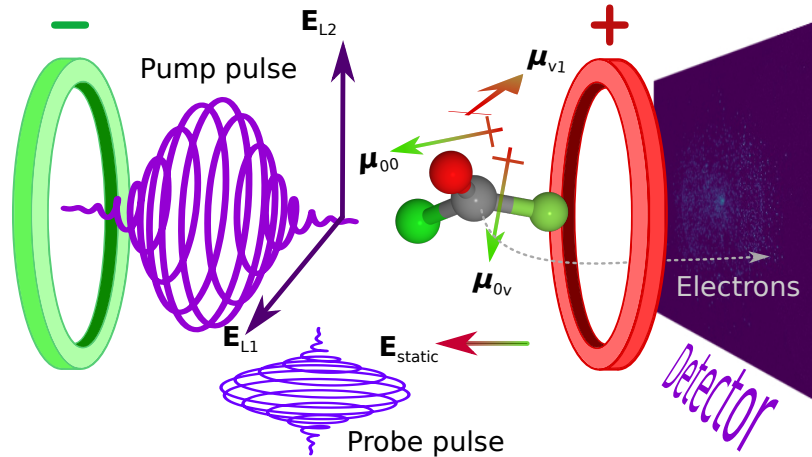


**Figure S1 Example of a field configuration to realize the proposed pump-probe spectroscopy in an experiment.** Electric field coils create the static electric field as well as the extraction field to image the photoelectrons resulting from the ionization of the planar molecules, taken to be COFC1 here. The UV pump pulse prepares the vibrational superposition via a Raman excitation, whereas the probe pulse ionizes the (time-dependent) superposition.



## B. Minimum number of fields to realize enantiomeric excess

To produce a broken parity, chiral state in a molecule, we need to create a superposition state from two (or more) levels of opposite parity [20]. One example of such states can be the vibrational states of the molecule, for instance the ground ( $|0\rangle$ ) and first excited ( $|1\rangle$ ) states of the out-of-plane (OOP) vibration of the COFCl molecule (for definition of the OOP coordinate see also Fig. S3). Let us assume the molecule to be initially in state  $|0\rangle$ . The superposition state after the excitation, for a single molecule with a particular orientation in space, is given by

$$|\psi(t)\rangle \approx |0\rangle + c_1^{(n)} \exp(-i\omega_{01}t)|1\rangle, \quad (1)$$

where  $\hbar\omega_{01}$  the energy difference between the two levels. The coefficients  $c_1^{(n)}$  are calculated with time-dependent perturbation theory of order  $n$ ,

$$c_1^{(n)}(t) = -\frac{i}{\hbar} \sum_{v \neq 1} \int_{t''}^t dt' \langle 1 | \hat{H}_{\text{int}}(t') | v \rangle \exp[-i\omega_{v1}(t' - t'')] c_v^{(n-1)}(t'). \quad (2)$$

Here,  $\hbar\omega_{v1}$  is the energy difference between the vibrational states  $|v \neq 1\rangle$  and  $|1\rangle$ . In particular, we consider direct excitation of the vibrational state  $|1\rangle$  with an IR-pulse, which corresponds to first order perturbation theory ( $n = 1$ ), and, alternatively, UV Raman excitation via virtual excited states, which is described by second order perturbation theory ( $n = 2$ ). The laser-molecule interaction is given by

$$\hat{H}_{\text{int}}(t) = -\mathbf{E}(t) \mathcal{R}(\varphi, \theta, \chi) \hat{\boldsymbol{\mu}}, \quad (3)$$

where  $\hat{\boldsymbol{\mu}}$  is the dipole moment in the molecular frame,  $\mathbf{E}(t)$  the electric field in the laboratory frame, and  $\mathcal{R}$  the rotation matrix connecting the two frames and depending on the Euler angles  $\phi, \theta, \chi$ ,

$$\mathcal{R}(\phi, \theta, \chi) = \underbrace{\begin{pmatrix} \cos(\chi) & -\sin(\chi) & 0 \\ \sin(\chi) & \cos(\chi) & 0 \\ 0 & 0 & 1 \end{pmatrix}}_{\mathcal{R}_\chi} \cdot \underbrace{\begin{pmatrix} 1 & 0 & 0 \\ 0 & \cos(\theta) & -\sin(\theta) \\ 0 & \sin(\theta) & \cos(\theta) \end{pmatrix}}_{\mathcal{R}_\theta} \cdot \underbrace{\begin{pmatrix} \cos(\phi) & -\sin(\phi) & 0 \\ \sin(\phi) & \cos(\phi) & 0 \\ 0 & 0 & 1 \end{pmatrix}}_{\mathcal{R}_\phi}. \quad (4)$$

For excitation with an IR pulse ( $n = 1$ ) or a Raman pulse ( $n = 2$ ), inserting Eq. (3) into Eq. (2) allows us to separate  $c_1^{(n)}$  into

$$c_1^{(n)}(t) = \prod_{k=1}^n \left( \mathbf{E}_k \cdot \mathcal{R}(\varphi, \theta, \chi) \boldsymbol{\mu}_k \right) \tilde{c}_1^{(n)}(t), \quad (5)$$

where  $\tilde{c}_1^{(n)}(t)$  does not depend on the Euler angles and is calculated in detail in Sec. IC. The angular dependence is expressed by the product  $\prod_{k=1}^n \left( \mathbf{E}_k \cdot \mathcal{R}(\varphi, \theta, \chi) \boldsymbol{\mu}_k \right)$ , where  $\mathbf{E}_k$  denotes the polarization direction and amplitude of the field responsible for the  $k$ th order interaction, and  $\boldsymbol{\mu}_k = \langle v' | \hat{\boldsymbol{\mu}} | v \rangle$  is the corresponding transition matrix element. The time-dependent part  $\tilde{c}_1^{(n)}(t)$  does not depend on the Euler angles and is calculated in detail in Sec. I.C. For simplicity, we assume here that in case of the UV Raman excitation the coefficients  $c_1^{(n)}(t)$  result from a single intermediate state  $|v\rangle$ . A more general derivation of  $c_1^{(n)}(t)$ , including the sum over all intermediate states  $|v\rangle$ , is presented below in Sec. IC.

Observables for a molecule with given orientation are obtained as

$$\langle \mathcal{O} \rangle(t) = \langle \psi(t) | \hat{\mathcal{O}} | \psi(t) \rangle = \langle 0 | \hat{\mathcal{O}} | 0 \rangle + |c_1^{(n)}|^2 \langle 1 | \hat{\mathcal{O}} | 1 \rangle + 2 \langle 0 | \hat{\mathcal{O}} | 1 \rangle \cdot \text{Re} \left[ c_1^{(n)} \exp(-i\omega_{01}t) \right]. \quad (6)$$

We are interested in observables that are sensitive to the coherence of the state and assume without loss of generality  $\langle 0 | \hat{\mathcal{O}} | 0 \rangle = \langle 1 | \hat{\mathcal{O}} | 1 \rangle = 0$  and  $\langle 0 | \hat{\mathcal{O}} | 1 \rangle \neq 0$ . Then

$$\langle \mathcal{O} \rangle(t) = 2|c_1^{(n)}| \langle 0 | \hat{\mathcal{O}} | 1 \rangle \cos(\omega_{01}t + \tilde{\varphi}_1) \quad (7)$$

with  $c_1^{(n)} = |c_1^{(n)}| \cdot \exp(-i\tilde{\varphi}_1)$ . In order to relate  $\langle \mathcal{O} \rangle(t)$ , i.e., the signal produced by a single molecule at a given orientation, to the macroscopic response of the system, we need to average over all the orientations that a molecule in the gaseous sample can take. We describe the rotational average classically,

$$\langle \langle \mathcal{O} \rangle \rangle(t) = \int d\Omega P(\phi, \theta, \chi) \langle \mathcal{O} \rangle(t), \quad (8)$$

where  $\int d\Omega = \int_0^{2\pi} d\phi \int_0^\pi \sin\theta d\theta \int_0^{2\pi} d\chi$  denotes the integration over the Euler angles. In the presence of a static electric field  $\mathbf{E}_{\text{static}}$ , the orientational distribution of the molecules in thermal equilibrium at temperature  $T$  is given by

$$P(\phi, \theta, \chi) = \frac{1}{Q} \exp\left(-\frac{E_{\text{rot}}}{k_{\text{B}}T}\right) \exp\left(\frac{\mathbf{E}_{\text{static}} \cdot \mathcal{R}(\phi, \theta, \chi)\boldsymbol{\mu}_{00}}{k_{\text{B}}T}\right), \quad (9)$$

where  $Q$  is the partition function,  $E_{\text{rot}}$  the (classical) rotational energy and  $\boldsymbol{\mu}_{00}$  the permanent dipole moment of the molecule. Classical rotational averaging is valid as long as the rotational spectrum is not resolved, i.e., for time-scales shorter than the rotational period. The rotational period of the molecules around the principle axis  $\alpha$  ( $\alpha = a, b, c$ ) can be estimated as  $\tau_{\text{rot},\alpha} \propto B_\alpha^{-1}$ , where  $B_\alpha$  is the rotational constant for rotation about that principle axis. The shortest rotational period corresponds to the largest rotational constant,  $B_a = A$ . For COFCl,  $A = 12$  GHz, and thus  $\tau_{\text{rot},a} = 8$  ps. This is much longer than typical pump-probe delays of a few hundred femtoseconds. Moreover, we neglect a possible time-dependence of  $P(\phi, \theta, \chi)$ . This is justified if the interaction with the pump pulse is too weak to create a rotational wavepacket that causes pronounced alignment. To test this assumption, we have calculated the classical alignment factors of COFCl with a Monte-Carlo simulation for classical rigid rotors. We have found that a pump pulse with an intensity of  $10^{13}$  W/cm<sup>2</sup> and a FWHM of 150 fs indeed does not create molecular alignment within several ps, so that the assumption of a time-independent angular distribution function is justified.

Expanding the Boltzmann distribution to first order in the static field amplitude, the orientational distribution can be approximated by

$$P(\phi, \theta, \chi) \approx P^{(0)} \left(1 + P^{(1)}(\phi, \theta, \chi)\right), \quad (10)$$

where  $P^{(0)} = \frac{1}{Q} \exp\left(-\frac{E_{\text{rot}}}{k_{\text{B}}T}\right)$  is the field-free isotropic distribution which does not depend on the Euler angles, while

$$P^{(1)}(\phi, \theta, \chi) = \frac{\mathbf{E}_{\text{static}} \cdot \mathcal{R}(\phi, \theta, \chi)\boldsymbol{\mu}_{00}}{k_{\text{B}}T} \quad (11)$$

describes the first-order orientation produced by the static field. Rotational Debye temperatures for COFCl, below which the thermal ensemble cannot be described classically anymore, are around 0.5 K. For rotational temperatures above 1 K, a classical treatment is thus well justified.

As a result, the orientational average for an observable  $\mathcal{O}$  is given by

$$\langle\langle \mathcal{O} \rangle\rangle \propto 2|\tilde{c}_1^{(n)}(t)|\langle 0|\hat{\mathcal{O}}|1\rangle \cos(\omega_{01}t + \tilde{\varphi}_1) \int d\Omega \left(\prod_{k=1}^n (\mathbf{E}_k \cdot \mathcal{R}(\phi, \theta, \chi)\boldsymbol{\mu}_k)\right) \left[1 + \frac{\mathbf{E}_{n+1} \cdot \mathcal{R}(\phi, \theta, \chi)\boldsymbol{\mu}_{n+1}}{k_{\text{B}}T}\right], \quad (12)$$

with  $\mathbf{E}_{n+1} = \mathbf{E}_{\text{static}}$  and  $\boldsymbol{\mu}_{n+1} = \boldsymbol{\mu}_{00}$ . Evaluating the integrals according to Ref. [22], we find, depending on the number of external fields,

$N=1$ :  $\int d\Omega (\mathbf{E}_1 \cdot \mathcal{R}(\phi, \theta, \chi)\boldsymbol{\mu}_1) = 0$ . This means that a single IR pulse (with  $\mathbf{E}_1 = \mathbf{E}_{L1}$  and  $\boldsymbol{\mu}_1 = \boldsymbol{\mu}_{01}$  in the notation of the main text), inducing the transition  $|0\rangle \rightarrow |1\rangle$ , cannot produce a chiral signature for the ensemble,

$N=2$ :  $\int d\Omega \prod_{k=1}^2 (\mathbf{E}_k \cdot \mathcal{R}(\phi, \theta, \chi)\boldsymbol{\mu}_k) \propto (\mathbf{E}_1 \cdot \mathbf{E}_2)(\boldsymbol{\mu}_1 \cdot \boldsymbol{\mu}_2)$ . Such a configuration could be realized in two different ways with both resulting, however, in a vanishing integral:

- IR excitation  $|0\rangle \rightarrow |1\rangle$  combined with static field orientation ( $\mathbf{E}_1 = \mathbf{E}_{L1}$ ,  $\mathbf{E}_2 = \mathbf{E}_{\text{static}}$ ,  $\boldsymbol{\mu}_1 = \boldsymbol{\mu}_{01}$ , and  $\boldsymbol{\mu}_2 = \boldsymbol{\mu}_{00}$  in the notation of the main text). The integral vanishes because the permanent dipole moment  $\boldsymbol{\mu}_{00}$  is in the molecular plane, whereas the transition dipole moment  $\boldsymbol{\mu}_{01}$  is orthogonal to the molecular plane and therefore  $(\boldsymbol{\mu}_{00} \cdot \boldsymbol{\mu}_{01}) = 0$ .
- Raman excitation  $|0\rangle \rightarrow |1\rangle$  without static field also does not yield a chiral signal ( $\mathbf{E}_1 = \mathbf{E}_{L1}$ ,  $\mathbf{E}_2 = \mathbf{E}_{L2}$ ,  $\boldsymbol{\mu}_1 = \boldsymbol{\mu}_{0v}$ , and  $\boldsymbol{\mu}_2 = \boldsymbol{\mu}_{v1}$  in the notation of the main text). The integrand vanishes because the two transition dipole moments are necessarily orthogonal to each other, as explained in more detail below in Section ID.

$N=3$ :  $\int d\Omega \prod_{k=1}^3 (\mathbf{E}_k \cdot \mathcal{R}(\phi, \theta, \chi)\boldsymbol{\mu}_k) \propto (\mathbf{E}_1 \cdot [\mathbf{E}_2 \times \mathbf{E}_3])(\boldsymbol{\mu}_1 \cdot [\boldsymbol{\mu}_2 \times \boldsymbol{\mu}_3])$ . These triple products do not necessarily vanish, which is why  $N=3$  is the smallest number of fields that may result in a non-zero rotational average. It requires three orthogonal (permanent or transition) dipole moments, with their triple product changing sign under spatial inversion. One possibility to realize the corresponding field configuration is Raman excitation with circular polarization in the presence of a static electric field perpendicular to the polarization plane of the circularly polarized field.  $\mathbf{E}_1 = \mathbf{E}_{L1}$ ,  $\mathbf{E}_2 = \mathbf{E}_{L2}$ ,  $\mathbf{E}_3 = \mathbf{E}_{\text{static}}$ ,  $\boldsymbol{\mu}_1 = \boldsymbol{\mu}_{0v}$ ,  $\boldsymbol{\mu}_2 = \boldsymbol{\mu}_{v1}$ , and  $\boldsymbol{\mu}_3 = \boldsymbol{\mu}_{00}$  in the notation of the main text.

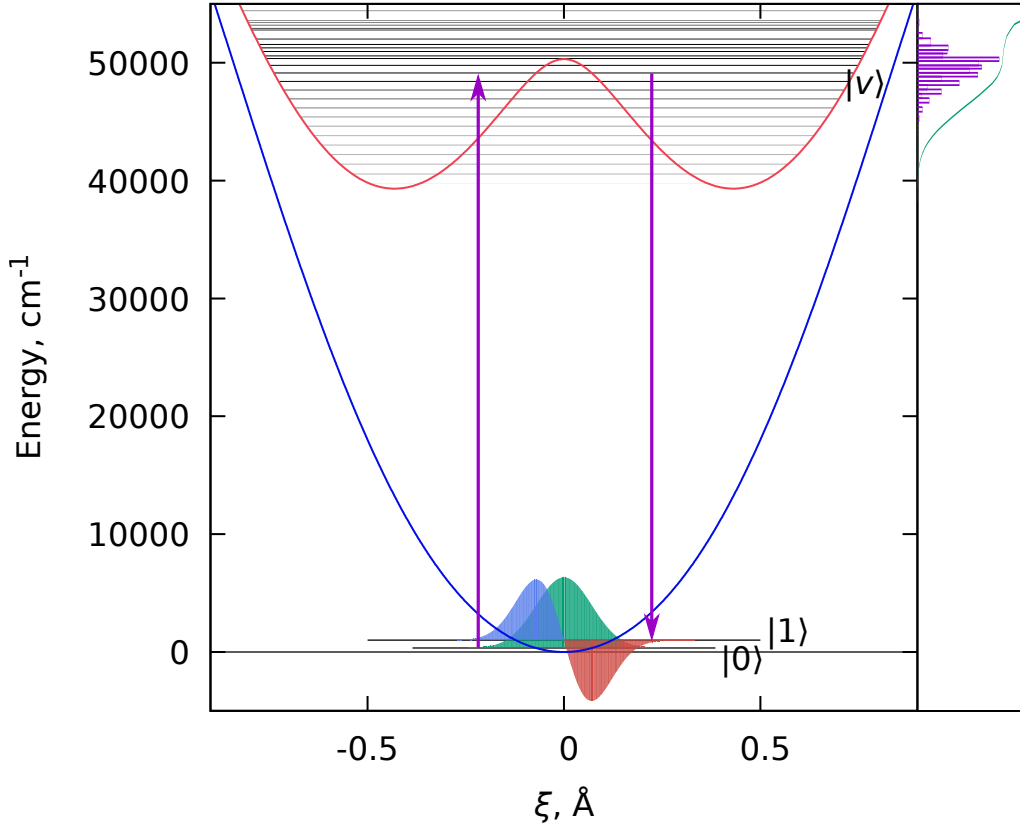


**Figure S2 Raman excitation of vibrational states for COFCl:** Ground and excited electronic potential surfaces along the out-of-plane coordinate  $\xi$  with vibrational levels (data shown for the example of the COFCl molecule). The purple arrows indicate the Raman excitation by the electric fields  $\mathbf{E}_{L1}$  and  $\mathbf{E}_{L2}$ . The figure also shows the vibrational eigenfunctions of COFCl, which is shown in more detail in Fig. S4.

### C. Magnitude of the induced enantiomeric excess

After clarifying the conditions for observing enantiomeric excess in a sample of randomly oriented molecules, we now estimate its magnitude. To this end, we utilize time-dependent perturbation theory (TDPT). The electric field driving the Raman excitation is given by

$$\mathbf{E}(t) = E_L \cdot (\mathbf{n}_1 \cos(\omega_L t + \varphi_1) + \mathbf{n}_2 \cos(\omega_L t + \varphi_2)) \cdot \exp\left(-\frac{t^2}{\tau^2}\right) \quad (13)$$

with  $\mathbf{E}_{L1} = E_L \cdot \mathbf{n}_1$  and  $\mathbf{E}_{L2} = E_L \cdot \mathbf{n}_2$ . Here,  $E_L$  is the electric field peak amplitude,  $\mathbf{n}$  and  $\varphi$  are the polarization axes and phases,  $\omega_L$  is the pulse carrier frequency, and  $\tau$  the pulse duration, related to the full width at half maximum (FWHM) by  $\text{FWHM} = 2\sqrt{\ln(2)}\tau$ . We consider Raman excitation from the ground to the first excited state of the out-of-plane vibration in the electronic ground state via vibronically excited states  $|v\rangle$ ,  $|0\rangle \rightarrow |v\rangle \rightarrow |1\rangle$ , see Fig. S2. This requires TDPT to second order, with the corresponding wavefunction given by

$$|\psi\rangle(t) = |0\rangle + c_1^{(2)}(t) \exp(-i\omega_0 t) |1\rangle + \sum_v c_v^{(1)}(t) \exp(-i\omega_v t) |v\rangle,$$

where  $\omega_{lm} = (E_m - E_l)/\hbar$  is the angular frequency of the  $|l\rangle \rightarrow |m\rangle$  transition. Invoking the rotating wave approximation, the expansion coefficients become

$$\begin{aligned} c_m^{(n+1)}(t) &= -i \sum_{l \neq m} \frac{\overbrace{\langle m | \hat{\boldsymbol{\mu}} | l \rangle}^{\boldsymbol{\mu}_{lm} = \boldsymbol{\mu}_{ml}}}{\hbar} \int_{-\infty}^t \mathbf{E}(t') \cdot \exp(i\omega_{lm}t') \cdot c_l^{(n)}(t') dt' \\ &\approx -i \sum_{l \neq m} \frac{\mathcal{R}\boldsymbol{\mu}_{lm} E_L}{2\hbar} (\mathbf{n}_1 \exp[-i \operatorname{sgn}(\omega_{lm})\varphi_1] + \mathbf{n}_2 \exp[-i \operatorname{sgn}(\omega_{lm})\varphi_2]) \\ &\quad \cdot \int_{-\infty}^t \exp\left[-\frac{t'^2}{\tau^2} - i\Delta_{lm}t'\right] \cdot c_l^{(n)}(t') dt', \end{aligned} \quad (14)$$

where  $\Delta_{lm} = \omega_{lm} - \operatorname{sgn}(\omega_{lm}) \cdot \omega_L$  is the detuning and  $\boldsymbol{\mu}_{lm}$  the transition dipole moment in the molecular frame, and  $\mathcal{R} = \mathcal{R}(\phi, \theta, \chi)$  is the rotation matrix (Eq. (4)), transforming the molecular frame into the laboratory frame. Evaluation to first order yields the coefficients of the virtual states  $|v\rangle$ ,

$$c_v^{(1)}(t) = -i \frac{E_L}{2\hbar} \{\mathcal{R}\boldsymbol{\mu}_{0v} (\mathbf{n}_1 \exp(-i\varphi_1) + \mathbf{n}_2 \exp(-i\varphi_2))\} \cdot \frac{\sqrt{\pi}\tau}{2} \left[1 + \operatorname{erf}\left(\frac{t}{\tau} + i\frac{\tau \cdot \Delta_{0v}}{2}\right)\right] \cdot \exp\left(-\frac{\tau^2 \Delta_{0v}^2}{4}\right),$$

where  $\exp\left(-\frac{\tau^2 \Delta_{0v}^2}{4}\right)$  represents the spectral profile of the Gaussian-shaped laser pulse. The second order coefficient cannot be evaluated analytically for non-vanishing detuning. We therefore estimate it approximately for zero detunings and account for the spectral pulse profile by multiplication with the two exponents of the form  $\exp\left(-\frac{\tau^2 \Delta^2}{4}\right)$  afterwards. This procedure is equivalent to treating the excitation as resonant absorption at the specific transition frequencies within the broad Gaussian spectrum of the pulse. With the time integral of the form

$$\int_{-\infty}^x \exp(-q^2)(1 + \operatorname{erf}(q))dq = \frac{\sqrt{\pi}}{4}(1 + \operatorname{erf}(x))^2,$$

this results in

$$\begin{aligned} c_1^{(2)}(t) &\approx -\sum_v \frac{\pi\tau^2}{4} \left(1 + \operatorname{erf}\left(\frac{t}{\tau}\right)\right)^2 \cdot \frac{E_L^2}{4\hbar^2} \cdot \{\mathcal{R}\boldsymbol{\mu}_{0v} (\mathbf{n}_1 \exp(-i\varphi_1) + \mathbf{n}_2 \exp(-i\varphi_2))\} \\ &\quad \cdot \{\mathcal{R}\boldsymbol{\mu}_{v1} (\mathbf{n}_1 \exp(+i\varphi_1) + \mathbf{n}_2 \exp(+i\varphi_2))\} \cdot \exp\left(-\frac{\tau^2 \Delta_{0v}^2}{4} - \frac{\tau^2 \Delta_{1v}^2}{4}\right). \end{aligned} \quad (15)$$

Inserting Eq. (15) into Eq. (12) yields rotationally averaged expectation values in second order TDPT,

$$\begin{aligned} \langle\langle \mathcal{O} \rangle\rangle(t) &= \int_0^{2\pi} d\phi \int_0^\pi \sin(\theta) d\theta \int_0^{2\pi} d\chi \langle \mathcal{O} \rangle(t, \phi, \theta, \chi) P(\phi, \theta, \chi) \\ &= 2\langle 0 | \hat{\mathcal{O}} | 1 \rangle \sin(\varphi_2 - \varphi_1) \sin(\omega_{01}t) E_L^2 E_{\text{static}} \frac{\pi\tau^2}{48\hbar^2 k_B T} (1 + \operatorname{erf}(t/\tau))^2 \\ &\quad \cdot \sum_v \exp\left(-(\tau^2 \Delta_{0v}^2 + \tau^2 \Delta_{1v}^2)/4\right) (\boldsymbol{\mu}_{00} \cdot [\boldsymbol{\mu}_{0v} \times \boldsymbol{\mu}_{1v}]) (\mathbf{n}_0 \cdot [\mathbf{n}_1 \times \mathbf{n}_2]). \end{aligned} \quad (16)$$

Equation (16) reveals how to maximize enantiomeric excess: The Raman pulse should be circularly polarized since  $|\sin(\varphi_2 - \varphi_1)| = 1$  is maximal for  $|\varphi_2 - \varphi_1| = \pi/2$ , and the static electric field and polarization axes should all be mutually orthogonal to maximize  $\mathbf{n}_0 \cdot [\mathbf{n}_1 \times \mathbf{n}_2] = 1$ .

#### D. Symmetry considerations

In this Section, we employ symmetry arguments to determine which components of the dipole and transition dipole moments  $\boldsymbol{\mu}_{00}$ ,  $\boldsymbol{\mu}_{0v}$  and  $\boldsymbol{\mu}_{v1}$  are non-zero. We consider planar molecules of  $C_s$  symmetry, with the  $ab$ -plane as symmetry plane and the molecular  $c$ -axis perpendicular to the symmetry-plane, then, the molecular axes  $a, b \in A'$  and  $c \in A''$ .

The Cartesian components of the molecular dipole moments are the projections onto the molecular axes,  $\mu^a \propto a$ ,  $\mu^b \propto b$ ,  $\mu^c \propto c$ , and thus transform as the molecular axis  $a$ ,  $b$  and  $c$ . In order to determine the non-zero components of the dipole and transition dipole moments, we separate the OOP vibronic states  $|0\rangle$ ,  $|1\rangle$ , and  $|v\rangle$  into their vibrational and electronic part,

$$|0\rangle = |0\rangle_{\text{vib}}|g\rangle_{\text{el}} , |1\rangle = |1\rangle_{\text{vib}}|g\rangle_{\text{el}} , |v\rangle = |v\rangle_{\text{vib}}|e\rangle_{\text{el}} .$$

The out-of-plane motion has  $A''$  symmetry, which means that the symmetry of the vibrational states along the OOP coordinate is  $\Gamma(|0\rangle_{\text{vib}}) = A'$  and  $\Gamma(|1\rangle_{\text{vib}}) = A''$ , i.e. the ground vibrational state is symmetric while the first excited state is anti-symmetric. Likewise, for the vibrational wavefunctions in the excited electronic state  $\Gamma(|v\rangle_{\text{vib}})$  is either  $A'$  or  $A''$  for even  $v$  and odd  $v$ , respectively.

The components  $i, j, k = a, b, c$  of the dipole and transition dipole moments are then

$$\begin{aligned} \mu_{00}^i &= \langle 0|\hat{\mu}^i|0\rangle = \langle 0|_{\text{vib}}\langle g|_{\text{el}}\hat{\mu}^i|g\rangle_{\text{el}}|0\rangle_{\text{vib}} , \\ \mu_{0v}^j &= \langle 0|\hat{\mu}^j|v\rangle = \langle 0|_{\text{vib}}\langle g|_{\text{el}}\hat{\mu}^j|e\rangle_{\text{el}}|v\rangle_{\text{vib}} , \\ \mu_{v1}^k &= \langle v|\hat{\mu}^k|1\rangle = \langle v|_{\text{vib}}\langle e|_{\text{el}}\hat{\mu}^k|g\rangle_{\text{el}}|1\rangle_{\text{vib}} . \end{aligned}$$

For each of the components to be nonzero, the product of the respective representations has to be fully symmetric, i.e. transform according to  $A'$  ( $\Gamma_1 \otimes \Gamma_2 \otimes \dots \otimes \Gamma_N = A'$ ). Since, for  $C_s$  symmetry,  $A' \otimes A' = A'' \otimes A'' = A'$ , and  $A' \otimes A'' = A'' \otimes A' = A''$ , this translates into

$$\begin{aligned} \Gamma(\mu_{00}^i) &= \overbrace{\Gamma(|0\rangle_{\text{vib}})}^{A'} \otimes \overbrace{\Gamma(|g\rangle_{\text{el}})}^{A'} \otimes \Gamma(\hat{\mu}^i) \otimes \overbrace{\Gamma(|g\rangle_{\text{el}})}^{A'} \otimes \overbrace{\Gamma(|0\rangle_{\text{vib}})}^{A'} = \Gamma(\hat{\mu}^i) , \\ \Gamma(\mu_{0v}^j) &= \overbrace{\Gamma(|0\rangle_{\text{vib}})}^{A'} \otimes \overbrace{\Gamma(|g\rangle_{\text{el}})}^{A'} \otimes \Gamma(\hat{\mu}^j) \otimes \overbrace{\Gamma(|e\rangle_{\text{el}})}^{A''} \otimes \Gamma(|v\rangle_{\text{vib}}) = \Gamma(\hat{\mu}^j) \otimes \Gamma(|v\rangle_{\text{vib}}) \otimes A'' , \\ \Gamma(\mu_{v1}^k) &= \Gamma(|v\rangle_{\text{vib}}) \otimes \overbrace{\Gamma(|e\rangle_{\text{el}})}^{A''} \otimes \Gamma(\hat{\mu}^k) \otimes \overbrace{\Gamma(|g\rangle_{\text{el}})}^{A'} \otimes \overbrace{\Gamma(|1\rangle_{\text{vib}})}^{A''} = \Gamma(\hat{\mu}^k) \otimes \Gamma(|v\rangle_{\text{vib}}) \otimes A' . \end{aligned}$$

The excited electronic state is antisymmetric ( $\Gamma(|e\rangle_{\text{el}}) = A''$ ) because the electronic transition is  $n \rightarrow \pi^*$ , and the  $\pi$ -orbitals are antisymmetric with respect to the plane of the molecule. The symmetry of dipole moment components is the same as for the molecular frame axes, i.e.,  $\mu^a, \mu^b \in A'$ , whilst  $\mu^c \in A''$ . Thus, for the permanent dipole we have only  $\mu_{00}^a$  and  $\mu_{00}^b$  available for being nonzero, and  $\mu_{00}^c = 0$ . If the virtual state is symmetric  $\Gamma(|v\rangle_{\text{vib}}) = A'$ , then the requirement is  $\Gamma(\mu_{0v}^j) = \Gamma(\hat{\mu}^j) \otimes A''$  and  $\Gamma(\mu_{v1}^k) = \Gamma(\hat{\mu}^k) \otimes A'$ . These conditions can be fulfilled if  $j = c$  and  $k = a, b$ . Similarly, if  $\Gamma(|v\rangle_{\text{vib}}) = A''$ , then the conditions are inverted  $\Gamma(\mu_{0v}^j) = \Gamma(\hat{\mu}^j) \otimes A'$  and  $\Gamma(\mu_{v1}^k) = \Gamma(\hat{\mu}^k) \otimes A''$ , which is fulfilled by  $j = a, b$  and  $k = c$ .

Orientation-averaged enantiomeric excess requires the triple product

$$\boldsymbol{\mu}_{00} \cdot [\boldsymbol{\mu}_{0v} \times \boldsymbol{\mu}_{v1}] = \varepsilon_{ijk} \mu_{00}^i \mu_{0v}^j \mu_{v1}^k$$

to be nonzero where we have used Einstein notation with  $\varepsilon_{ijk}$  the Levi-Civita symbol, and  $i, j, k = a, b, c$ . Since  $\varepsilon_{ijk} \neq 0$  only for  $i \neq j \neq k \neq i$ , the product is given by three different dipole moment components and these must be allowed to be non-zero by symmetry. Therefore, the following combinations are allowed by symmetry:

- if  $\Gamma(|v\rangle_{\text{vib}}) = A'$ , then  $\mu_{00}^a \mu_{0v}^b \mu_{v1}^c$  and  $\mu_{00}^b \mu_{0v}^a \mu_{v1}^c$  can be nonzero,
- if  $\Gamma(|v\rangle_{\text{vib}}) = A''$ , then  $\mu_{00}^a \mu_{0v}^c \mu_{v1}^b$  and  $\mu_{00}^b \mu_{0v}^c \mu_{v1}^a$  can be nonzero.

## II. COMPUTATIONAL DETAILS FOR THE COFCL MOLECULE

### A. Electronic structure

The quantum-chemical computations were performed at the B3LYP/cc-pVTZ level of theory [38, 39, 40, 42] using the Orca 4 package [44]. The structure of COFCl was optimized in the ground electronic state, yielding the equilibrium structure of the molecule given in Table S1 below. The harmonic frequency calculations confirmed the minimum. The ten lowest excited states were computed using time-dependent density functional theory within the Tamm-Dancoff approximation [43].



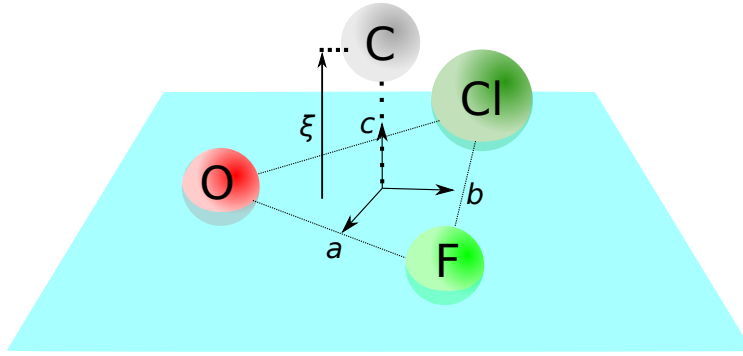


**Figure S3 Definition of the out-of-plane coordinate:** The molecular frame of the COFCl molecule is defined by the Cartesian coordinates  $a$ ,  $b$  and  $c$ . The out-of-plane coordinate  $\xi$  is given by the distance of the C-atom from the molecular plane spanned by the O, F, and Cl atoms.

The molecular frame was chosen such that all atoms lie in the  $ab$  plane. The out-of-plane (OOP) coordinate  $\xi$  corresponds the  $c$ -coordinate of the carbon atom, while all the other atoms (O, F, and Cl) are assumed to be frozen at their equilibrium positions, cf. Figure S3. For the ground, first excited, and ground ionic potential energy surfaces (PES), 100 points were computed with  $\xi \in [-0.9\text{\AA}, +0.9\text{\AA}]$ . Along with the energies, the ground state dipole moment  $\boldsymbol{\mu}_g(\xi) = \langle g(\xi) |_{\text{el}} \hat{\boldsymbol{\mu}} | g(\xi) \rangle_{\text{el}}$  and transition dipole moment  $\boldsymbol{\mu}_{ge}(\xi) = \langle g(\xi) |_{\text{el}} \hat{\boldsymbol{\mu}} | e(\xi) \rangle_{\text{el}}$  were computed at each  $\xi$ . To provide the quantum-chemical results here in a compact form, the energies  $V(\xi)$  and dipole moments  $\mu(\xi)$  were approximated by polynomials

$$f(\xi) = \sum_{n=0}^{15} f_n \xi^n. \quad (17)$$

The approximation results are presented below in Section IV, with the polynomial coefficients listed in Tables S2, S3, and S4. The quality of the approximation can be judged from Figures S9, S10, and S11.

## B. Vibrational structure

To calculate the vibrational states  $|n\rangle_{\text{vib}}$  of the OOP motion in the ground and first excited state, the grid points used in the electronic structure calculations were symmetrized along the mirror plane ( $\xi = 0$ ) and then interpolated to a uniform grid of 1000 points using cubic splines. The reduced mass for the OOP motion is given by

$$\mu = \frac{m(^{12}\text{C}) \cdot (m(^{16}\text{O}) + m(^{19}\text{F}) + m(^{35}\text{Cl}))}{m(^{12}\text{C}) + m(^{16}\text{O}) + m(^{19}\text{F}) + m(^{35}\text{Cl})}.$$

With these parameters, the vibrational Schrödinger was solved for both electronic manifolds, using a discrete-variable representation [45]. The vibrational states in the electronically excited state  $|v\rangle_{\text{vib}}$  were the symmetrized with respect to  $\xi = 0$ . From the resulting vibronic wavefunctions, the vibrationally averaged permanent dipole moments  $\boldsymbol{\mu}_{00} = \langle 0 |_{\text{vib}} \boldsymbol{\mu}_g(\xi) | 0 \rangle_{\text{vib}} = \langle 0 |_{\text{vib}} \langle g |_{\text{el}} | \hat{\boldsymbol{\mu}} | g \rangle_{\text{el}} | 0 \rangle_{\text{vib}}$  and transition dipole moments  $\boldsymbol{\mu}_{0v} = \langle 0 |_{\text{vib}} \boldsymbol{\mu}_{ge}(\xi) | v \rangle_{\text{vib}} = \langle 0 |_{\text{vib}} \langle g |_{\text{el}} | \hat{\boldsymbol{\mu}} | e \rangle_{\text{el}} | v \rangle_{\text{vib}}$ ,  $\boldsymbol{\mu}_{1v} = \langle 1 |_{\text{vib}} \boldsymbol{\mu}_{ge}(\xi) | v \rangle_{\text{vib}} = \langle 1 |_{\text{vib}} \langle g |_{\text{el}} | \hat{\boldsymbol{\mu}} | e \rangle_{\text{el}} | v \rangle_{\text{vib}}$ , corresponding to the Raman transition shown in Figure S2, were computed.

The quality of the vibronic states was evaluated by comparison with the available experimental data for COF<sup>35</sup>Cl. The experimental value for the out-of-plane fundamental vibrational transition ( $|0\rangle \rightarrow |1\rangle$ ) is  $667\text{ cm}^{-1}$ , the value obtained in our calculations was  $662\text{ cm}^{-1}$  (relative error of 1%). From the  $|\boldsymbol{\mu}_{0v}|^2$  values, the UV absorption spectrum was also calculated. The comparison with the available band shape from the MPI-Mainz UV/VIS Spectral Atlas [50] shows a good reproduction of the first UV band, cf Fig. S4.

## C. Vibrationally averaged photoelectron angular distributions

For the calculation of photoelectron angular distributions (PAD), we have extended the procedure of Refs. [29, 30] to explicitly account for the vibrational dynamics via vibrational averaging. Starting in the Born-Oppenheimer

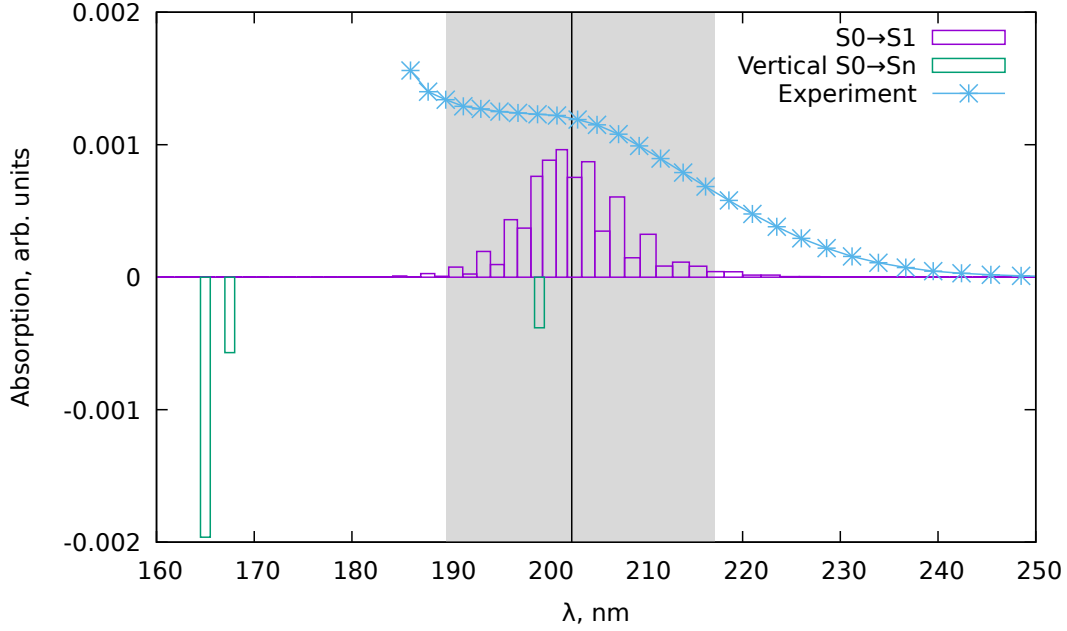


**Figure S4 Absorption spectrum of COFCl:** Experimental [50] (solid line with crosses) and calculated (violet boxes) vibronic absorption spectra of COFCl. The green boxes in the negative range illustrate positions and intensities of the vertical electronic spectrum computed from the equilibrium structure of the COFCl. The vertical line and the shaded area around it illustrate the position of the 4th harmonic of a Ti:Sa laser with a wavelength of 810 nm and the bandwidth of a Fourier-limited 10 fs pulse. The level of theory used was TDA-B3LYP/cc-pVTZ.

approximation, we write the vibronic state of the molecule as

$$|\psi\rangle(t) = \sum_j c_{j,g}(t) e^{-i\omega_{j,g}t} |j\rangle_{\text{vib}} |g\rangle_{\text{el}} + \sum_v c_{v,e}(t) e^{-i\omega_{v,e}t} |v\rangle_{\text{vib}} |e\rangle_{\text{el}} + \sum_{v'} c_{v',\mathbf{k}}(t) e^{-i\omega_{v',\mathbf{k}}t} |v'\rangle_{\text{vib}} |\mathbf{k}\rangle_{\text{el}}, \quad (18)$$

where  $|g\rangle_{\text{el}}$  refers to the electronic ground state,  $|e\rangle_{\text{el}}$  to the electronically excited state, and  $|\mathbf{k}\rangle_{\text{el}}$  is the electronic state of the ion after photoionization with  $\mathbf{k} = (k, \phi_k, \theta_k)$  the laboratory frame momentum of the emitted electron.  $|v\rangle_{\text{vib}}$  represent the vibrational eigenstates in the corresponding PES with eigenfrequencies  $\omega_{v,n}$ . The expansion coefficients of the electronic ground state,  $c_{j,g}(t) = \sum_n c_{j,g}^{(n)}(t)$  (with  $c_{j,g}^{(n)}(t)$  introduced in Sec. IC), describe the chiral vibrational wavepacket. We evaluate them up to second-order time-dependent perturbation theory according to Equation (14), describing the Raman excitation by the pump pulse. Here, we solve the second-order time integral numerically. Assuming one-photon ionization from the highest occupied molecular orbital by the circularly polarized XUV probe pulse  $\mathbf{E}_I$ , we calculate the ionic expansion coefficients in Equation (18) by third-order perturbation theory,

$$c_{v',\mathbf{k}}^{(3)}(t) = -i \sum_{j=0,1} \int_{-\infty}^t e^{i(\omega_{v',\mathbf{k}} - \omega_{j,g})t'} \langle v' |_{\text{vib}} \langle \mathbf{k} |_{\text{el}} \mathbf{E}_I(t') \cdot \mathcal{R}(\phi, \theta, \chi) \cdot \hat{\boldsymbol{\mu}} |g\rangle_{\text{el}} |j\rangle_{\text{vib}} c_{j,g}^{(2)}(t') dt', \quad (19)$$

where  $\mathcal{R}(\phi, \theta, \chi)$  transforms the molecule-fixed dipole operator into the laboratory-fixed frame of reference. Hence, the expansion coefficients depend on the orientation of the molecule, i.e.,  $c_{v,n}(t) \equiv c_{v,n}(t; \phi, \theta, \chi)$  for  $n = g, e, \mathbf{k}$ .

Equation (19) implies an integral over the vibrational coordinate,

$$\langle v' |_{\text{vib}} \langle \mathbf{k} |_{\text{el}} \hat{\boldsymbol{\mu}} |g\rangle_{\text{el}} |j\rangle_{\text{vib}} = \int \chi_{v',\mathbf{k}}^*(\xi) \boldsymbol{\mu}_{\mathbf{k}g}(\xi) \chi_{j,g}(\xi) d\xi,$$

where  $\chi_{j,g}(\xi)$  and  $\chi_{v',\mathbf{k}}(\xi)$  are the vibrational eigenfunctions in the neutral and ionic ground electronic states. In other words, the vibrational dynamics is taken into account by averaging over the parametric dependence of the electronic states on the nuclear coordinates, with the approximation that all nuclei are fixed except for the OOP motion, see Fig. S3. For a given, fixed value of the OOP coordinate  $\xi$ , we follow the procedure of Refs. [29, 30] to evaluate the electronic dipole matrix elements in Equation (19),  $\boldsymbol{\mu}_{\mathbf{k}g}(\xi) = \langle \mathbf{k}(\xi) |_{\text{el}} \hat{\boldsymbol{\mu}} |g(\xi)\rangle_{\text{el}}$ , by applying a single center expansion. This yields the transition dipole moments to the electronic continuum state of the ion in the frozen-core Hartree-Fock

approximation. The calculation is performed with the `ePolyScat` program. It requires the electronic ground state to be represented by a single Slater determinant [54, 55], which we calculate at the HF/aug-cc-pVTZ level of theory. Thus, the continuum dipole matrix elements are calculated for different values of  $\xi$  by manipulating the molecular geometry in the calculation of the ground state Slater determinant. This enables us to obtain vibronic transition dipole matrix elements in terms of the overlap of vibrational nuclear wavefunctions, calculated as described in Sec. II B, and the parametrized electronic dipole matrix elements. We use partial waves up to  $L = 80$  to represent the bound orbitals on the angular grid in order to ensure converged transition dipole matrix elements at photoelectron energies up to 20 eV.

In order to reduce the numerical effort in evaluating Equation (19), we approximate the shape of the ionizing pulse by  $\delta(t - t_I)$  and assume the PAD to display a Gaussian energy dependence, which is given by the ionizing pulse spectrum [56]. This neglects the energy dependence of the continuum dipole matrix elements. We have verified that this is a reasonable approximation as long as the probe pulse duration is significantly shorter than the oscillation period of enantiomeric excess, i.e., the ionization pulse is not longer than 5 fs. Of course, the latter is required in any case, in order to resolve the chiral vibrational motion.

For a single molecule with given orientation, the laboratory-frame PAD at time  $t$  for a photoelectron with momentum  $\mathbf{k}$  is given in terms of the ionic expansion coefficients,

$$\text{PAD}(t; \mathbf{k}; \phi, \theta, \chi) = \sum_{v'} \left| c_{v', \mathbf{k}}^{(3)}(t; \phi, \theta, \chi) \right|^2, \quad (20)$$

where the sum runs over all populated vibrational states  $v'$  in the ground electronic state of the ion. The orientation-averaged laboratory-frame PAD is then obtained by integrating over the Euler angles,

$$\langle \text{PAD} \rangle(t; \mathbf{k}) = \int_0^{2\pi} d\phi \int_0^{\pi} \sin\theta d\theta \int_0^{2\pi} d\chi P(\phi, \theta, \chi) \text{PAD}(t; \mathbf{k}; \phi, \theta, \chi), \quad (21)$$

where  $P(\phi, \theta, \chi)$  describes the orientational distribution of the molecules, including the effect of the static electric field, cf. Sec. IB. As explained in Sec. IB, it is well justified to take the orientational distribution to be time-independent — this applies also to duration of the probe pulse. The integral over molecular orientations in Equation (21) is evaluated numerically.

Photoelectron circular dichroism (PECD) is the forward-backward asymmetry visible in the dichroic difference of PADs upon ionization with left- and right-circularly polarized (LCP/RCP) light. We quantify PECD according to the convention of Ref. [24], i.e.

$$\langle \text{PECD} \rangle(t; \mathbf{k}) = \frac{\langle \text{PAD}^{\text{LCP}} \rangle(t; \mathbf{k}) - \langle \text{PAD}^{\text{RCP}} \rangle(t; \mathbf{k})}{(\langle \text{PAD}^{\text{LCP}} \rangle(t; \mathbf{k}) + \langle \text{PAD}^{\text{RCP}} \rangle(t; \mathbf{k}))/2}. \quad (22)$$

This convention is commonly used in experiments and often combined with an integration of the PADs over the forward and backward hemisphere [12, 25, 26, 27]. The latter can result in smaller values, if the individual hemispheres contain contributions to PECD with opposite signs, which cancel each other upon integration. In the proposed experiment, we observe almost complete cancellation of PECD inside the hemispheres with the pulse parameters given in the main text. In our understanding, this cancellation happens by chance for COFCl at the selected photoelectron energy, since there is no symmetry requirement that forces this cancellation to occur.

The orientation-averaged PADs are cylindrically symmetric due to the cylindrical symmetry of the proposed experimental setup (cf. Fig. S1). Hence, it does not matter if PECD is calculated from the PADs itself or from velocity map images (VMI), i.e. the projection of Eq. (22) onto the  $yz$ -plane. However, due to the orientation of the molecules by the static electric field, the dichroic differences are not antisymmetric with respect to the light propagation direction as it is the case for randomly oriented molecules. For completeness, Fig. S5 shows polar plots of the orientation-averaged laboratory frame PADs for the pump-probe delays that are marked in Fig. 3 of the main text, displaying PADs obtained with a left- and a right-circularly polarized probe pulse and their normalized dichroic difference.

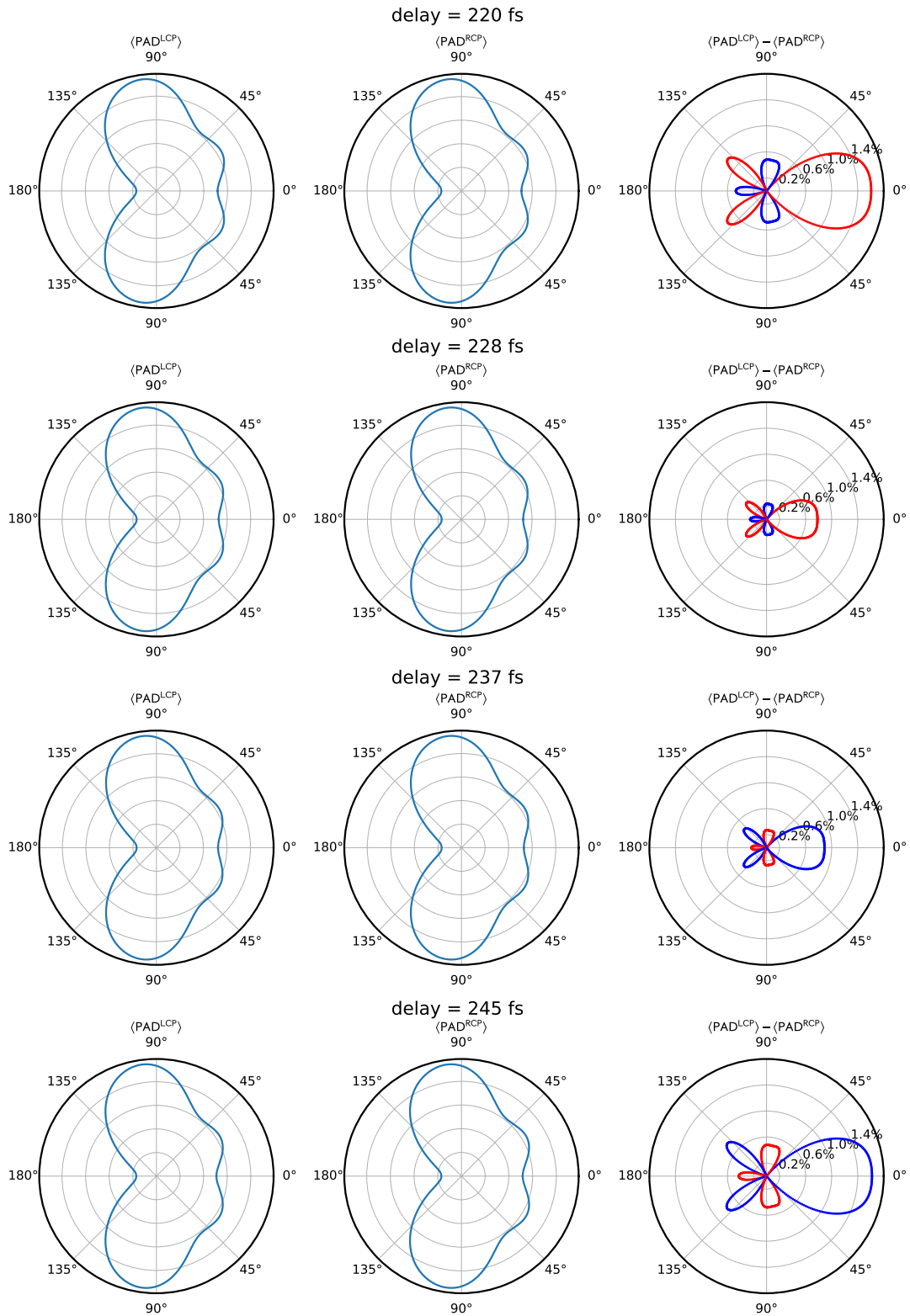


**Figure S5 Photoelectron angular distribution:** Polar plots of the orientation-averaged laboratory frame photoelectron angular distributions obtained with a left- and right-circularly polarized ionizing pulse and the corresponding dichroic difference where  $\theta_k$  is the polar angle of the photoelectron momentum. The latter has been normalized with respect to the mean value of the corresponding PADs according to Eq. (22). The simulation parameters are the same as for the results presented in Fig. 3 of the main text. The rows correspond to the time delays that are marked with dashed vertical lines in Fig. 3 of the main text. The dichroic difference in the right column is shown as absolute value in percent, while the sign is encoded in the color, i.e., red and blue corresponds to positive and negative values, respectively.

### III. DEPHASING AND RELAXATION TIMESCALES

An essential aspect of the ultrafast experiments is the decay time of the signal, because it limits the timescale over which the probe can monitor the effect induced by the pump pulse. Here, we consider mechanisms that may limit observation of the vibrational coherence. To observe the motion of the chiral wavepacket, at least one period of the out-of-plane vibration in COFCl, which is about 50 fs. Ideally, the shortest dephasing time should be at least an order of magnitude larger. Since we also assume pump and probe not to overlap in time, all the dephasing times should be larger than 1 ps in order to exclude detrimental effects of dephasing in the proposed experiment.

#### A. Collisional dephasing

Ultrafast experiments typically use either an effusive beam or supersonic expansion, both of which are hard to model. Instead, one can estimate an upper bound to the collision frequency by using a simple equilibrium gas model at elevated temperatures.

The collisional frequency in the ideal gas at equilibrium is given by [59]

$$\frac{1}{\tau_{\text{coll}}} = 4\sigma \frac{P}{\sqrt{\pi m k_{\text{B}} T}},$$

where  $\tau_{\text{coll}}$  is the collision period,  $\sigma$  the collisional cross-section,  $m$  the mass of the molecule,  $P$  pressure,  $T$  temperature, and  $k_{\text{B}}$  Boltzmann's constant. The upper boundary for the  $\tau_{\text{coll}}$  can be estimated by taking the  $P = 1$  atm.,  $T = 300$  K,

and  $\sigma = \pi R^2$ , where  $R = \left( \overbrace{R(\text{Cl} \dots \text{O})}^{2.6} + \overbrace{R_{\text{vdW}}(\text{Cl})}^{1.8} + \overbrace{R_{\text{vdW}}(\text{O})}^{1.5} \right) / 2 \approx 3 \text{ \AA}$  with  $R(\text{Cl} \dots \text{O})$  being the distance between Cl and O in COFCl (the largest interatomic distance), and  $R_{\text{vdW}}$  are the van der Waals radii of the respective atoms [60]. Such estimation gives  $\tau_{\text{coll}} \approx 400$  ps, which is much greater than the desired limit of 1 ps.

#### B. Rotational dephasing

To estimate the timescale of rotational dephasing, we assume rotations and vibrations to be decoupled due to their different characteristic timescales and all vibrational-rotational transitions having the same transition matrix elements. The oscillation of the chiral observable  $\mathcal{O}$  (Eq. 16) at long times after the pump pulse ( $t \gg \tau$ , when  $(1 + \text{erf}(t/\tau)) \approx 2$ ) can be expressed as

$$I(t) = A \cdot \sin(\omega_{01} t),$$

where  $I$  is the intensity of the signal,  $\omega_{01}$  the vibrational transition frequency in the electronic ground state, and  $A$  amplitude of the observable's ( $\mathcal{O}$ ) oscillation. However, the vibrational coherence, induced by the laser pulse would include multiple rotational states. In the rigid rotor and harmonic oscillator (RRHO) approximation, the induced rovibrational transition frequency will be given as  $\omega = \omega_{01} + \delta\omega$ , where  $\delta\omega$  denotes the difference in the rotational frequencies of the pair of the coherent states. We approximate the rotational states of the asymmetric top by those of a spherical top: Each state  $|JKM\rangle$  with total momentum  $J = 0, 1, 2, \dots$ , and projections of the total momentum on the molecular and lab frames  $K, M = -J, -J+1, \dots, 0, \dots, J-1, J$  has an energy of  $hBJ(J+1)$ , where  $B = \frac{\hbar}{4\pi I}$  is the rotational constant, dependent on the moment of inertia  $I$ . The rotational energy levels for each  $J$  are  $(2J+1)^2$  times degenerate. We take the levels to be occupied according to Boltzmann distribution and assume that the classical regime is applicable, i.e., thermal fluctuations  $k_{\text{B}}T$  are more prominent than the difference between nearest quantum levels. With these assumptions, the predicted signal for the molecule in the specific initial and final rotational states will be given by

$$I = A \cdot \sin(\underbrace{\omega_{01} t}_{X=X(t)} + \delta\omega t) = A \cdot \sin(X + \delta\omega t).$$

Vibrational-rotational spectra of nonlinear molecules in the electric dipole approximation consist of three branches of transitions with different frequency shifts due to rotational state change:

- P-branch with  $\Delta J = -1$  ( $|J\rangle \rightarrow |J-1\rangle$ ):  $\delta\omega_{\text{P}} = -4\pi BJ$ ,
- Q-branch with  $\Delta J = 0$  ( $|J\rangle \rightarrow |J\rangle$ ):  $\delta\omega_{\text{Q}} = 0$ ,



- R-branch with  $\Delta J = +1$  ( $|J\rangle \rightarrow |J+1\rangle$ ):  $\delta\omega_R = 4\pi B(J+1)$ .

For the Raman transition, the P- and R-branches have to be replaced by the O-branch ( $|J\rangle \rightarrow |J-2\rangle$ ) and S-branch ( $|J\rangle \rightarrow |J+2\rangle$ ) but in the classical limit ( $\Delta E_{J \rightarrow J'} \approx J$ ) this will not change the final result.

The final signal will be a combination of interfering signals from each of the three branches,

$$I = \frac{1}{3} \left( \underbrace{\frac{A}{Z} \sum_{J=0}^{+\infty} w_J \sin(X - 4\pi B J t)}_{I_P} + \underbrace{\frac{A}{Z} \sin(X) \sum_{J=0}^{+\infty} w_J}_{I_Q} + \underbrace{\frac{A}{Z} \sum_{J=0}^{+\infty} w_J \sin(X + 4\pi B (J+1) t)}_{I_R} \right) = \frac{1}{3} \left( I_P + I_R + \underbrace{A \cdot \sin(X)}_{I_Q} \right).$$

In this approximation, the signal from the Q-branch does not depend on  $J$ , whilst the frequencies of the P- and R-branches depend linearly on  $J$ . To estimate  $I_P + I_R$ , we take the classical limit, replacing the sum  $\sum_{J=0}^{+\infty}$  by an integral  $\int_0^{+\infty} dJ$  and assuming  $J$  to be large enough such that  $J(J+1) \approx J^2$ ,  $(2J+1)^2 \approx 4J^2$  and  $J+1 \approx J$ . This gives

$$\begin{aligned} I_P + I_R &\approx \frac{4A}{Z} \int_{J=0}^{+\infty} J^2 \exp\left(-\frac{hB}{k_B T} J^2\right) \sin(X - 4\pi B J t) dJ + \frac{4A}{Z} \int_0^{+\infty} J^2 \exp\left(-\frac{hB}{k_B T} J^2\right) \sin(X + 4\pi B J t) dJ \\ &= \frac{4A}{Z} \int_{-\infty}^{+\infty} J^2 \exp\left(-\frac{hB}{k_B T} J^2\right) \sin(X + 4\pi B J t) dJ = \frac{4A}{Z} \frac{(I_+ - I_-)}{2i} \end{aligned}$$

with

$$I_+ = \int_{-\infty}^{+\infty} J^2 \exp\left(-\frac{hB}{k_B T} J^2 + iX + i4\pi B J t\right) dJ, \quad I_- = \int_{-\infty}^{+\infty} J^2 \exp\left(-\frac{hB}{k_B T} J^2 - iX - i4\pi B J t\right) dJ.$$

All the three integrals needed ( $Z$ ,  $I_{\pm}$ ) are easy to calculate:

$$\begin{aligned} Z &\approx 4 \int_{J=0}^{+\infty} J^2 \exp\left(-\frac{hB}{k_B T} J^2\right) dJ = \sqrt{\pi} \cdot \left(\frac{k_B T}{hB}\right)^{3/2}. \\ I_{\pm} &= \exp(\pm iX) \cdot Z \cdot \exp\left(-\frac{2\pi k_B T B t^2}{\hbar}\right) \cdot \left(\frac{1}{2} - (2\pi B t)^2\right), \end{aligned}$$

where for  $I_{\pm}$  we have used the substitution  $J \rightarrow j_{\pm} = J \mp \frac{ik_B T t}{\hbar}$ . When combining all the terms, we obtain

$$I(t) = \frac{1}{3} (I_P(t) + I_R(t) + I_Q(t)) = A \cdot \underbrace{\sin(\omega_0 t)}_X \cdot \underbrace{\frac{1}{3} \left(1 + 4 \exp\left(-\frac{2\pi k_B T B t^2}{\hbar}\right) \cdot \left(\frac{1}{2} - (2\pi B t)^2\right)\right)}_{\Xi(t)}. \quad (23)$$

The maximal value of  $\Xi(t)$  is one (for  $t = 0$ ), and the  $t = +\infty$  limit is  $\Xi(+\infty) = 1/3$ , which corresponds to a cancelation of the signals between P and R branches with only the Q branch left. A plot of  $\Xi(t)$  for the different rotational As an estimate of the rotational decoherence times, we can use the time of the half-decay  $\tau_{\text{rot},1/2}$  for the  $\Xi(t)$ , defined through the equation  $\Xi(\tau_{\text{rot},1/2}) = 2/3$ .

The Figure S7 shows the dependence of the  $\tau_{\text{rot},1/2}$  for COF<sup>35</sup>Cl molecule at the different rotational temperatures. A signal lasting longer than 1 ps is expected for rotational temperatures below 70 K. Such temperatures are easily achieved in molecular beam experiments. In the proposed experiment, they are needed also to ensure negligible thermal population in the excited vibrational level of the electronic ground state. We therefore conclude that rotational dephasing will not be relevant.

### C. Vibrational excitation intramolecular vibrational energy redistribution lifetime

Coupling of the degree of interest, the OOP vibration, to other vibrational modes will lead to intramolecular vibrational energy redistribution (IVR) and decay of the desired signal. To estimate the rate with which excitation in the OOP vibration decays into other vibrations due to anharmonic couplings, we have performed *ab initio* molecular dynamics (AIMD) simulations for COFCl. We have taken the  $\langle 0|\xi|1\rangle$  average structure obtained at the B3LYP/cc-pVTZ level of

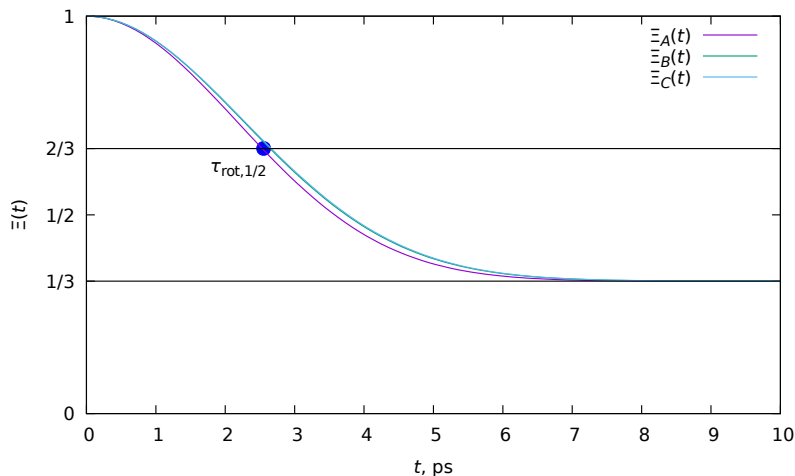


**Figure S6 Rotational dephasing:** Time-dependence of the rotational dephasing function  $\Xi(t)$  (Equation (23)) at rotational temperature of 10 K for three rotational constants of  $\text{COF}^{35}\text{Cl}$  molecule ( $A = 11830$  MHz,  $B = 5287$  MHz, and  $C = 3649$  MHz taken from Ref. [49]). The point  $\tau_{\text{rot},1/2}$  indicates the half-decay time for this  $\Xi(t)$ .

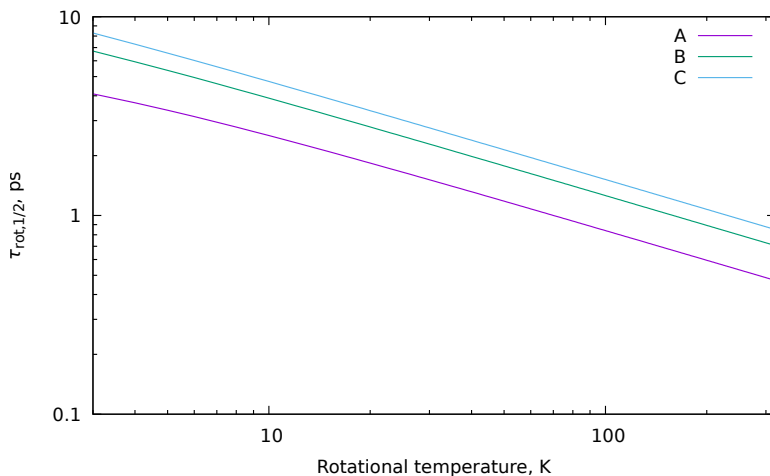


**Figure S7 Temperature dependence of the rotational dephasing:** The dependence of the half-decay times for the rotational dephasing function  $\Xi(t)$  (Equation (23)), as a function of rotational temperature for the  $\text{COF}^{35}\text{Cl}$  molecule with rotational constants  $A = 11830$  MHz,  $B = 5287$  MHz, and  $C = 3649$  MHz (values taken from Ref. [49]).

theory, cf. Table S1, as the initial structure for the simulations. Then, 28 AIMD trajectories with velocities generated from a Maxwell-Boltzmann distribution at 300 K were calculated for a duration of 0.5 ps with a time step of 0.1 fs, such that the trajectories covered approximately ten periods of OOP vibration in COFCl. The gradients were obtained at the B3LYP-D3/def2-SVP level of theory. From each trajectory, the evolution of the carbon displacement from the  $ab$ -plane,

$$\xi = \frac{\mathbf{r}_{\text{OC}} \cdot [\mathbf{r}_{\text{OF}} \times \mathbf{r}_{\text{OCl}}]}{\|[\mathbf{r}_{\text{OF}} \times \mathbf{r}_{\text{OCl}}]\|}, \quad (24)$$

was extracted. The results are shown in Figure S8. The average time dependence of this coordinate was fitted to a function describing an harmonic oscillator with friction,

$$\xi(t) = A_\xi \cdot \sin(\omega_{01}t + \phi) \cdot \exp(-t/\tau_{\text{IVR}}) \quad (25)$$

with  $A_\xi$  the vibrational amplitude,  $\phi$  the phase and  $\tau_{\text{IVR}}$  an estimate of the IVR relaxation time, also shown in Figure S8. The latter was found to be  $\tau_{\text{IVR}} = 3.6 \pm 0.2$  ps. This suggests that IVR in COFCl is about two orders of

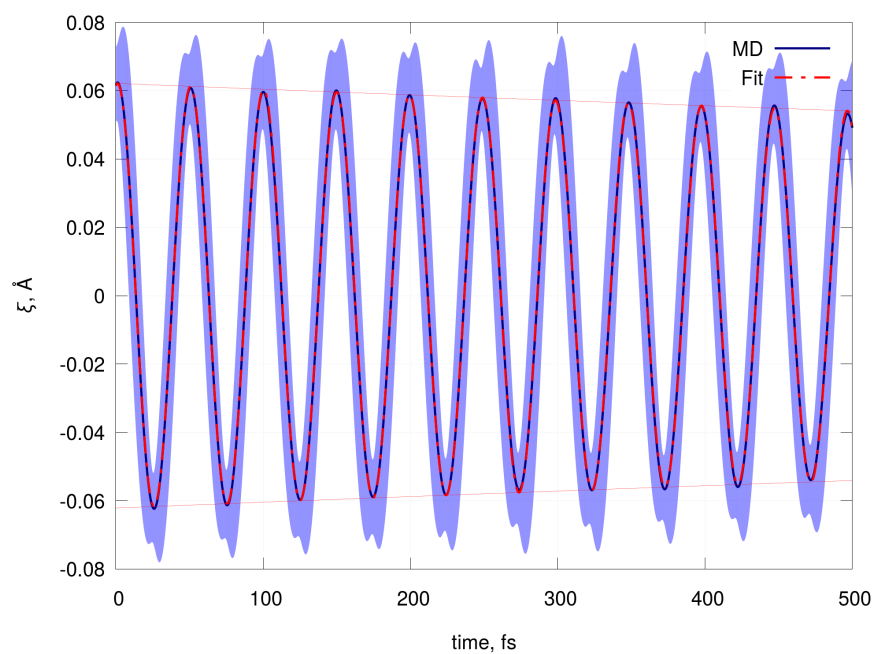


**Figure S8 Decay of the vibrational amplitude due to vibrational energy redistribution:** Average displacement of the  $\xi$  out-of-plane coordinate in COFCl (solid blue line) obtained with AIMD trajectory simulations at the B3LYP-D3/def2-SVP level of theory, cf. Equation (24). The average is fitted to Equation (25) (thick red line) which results in an estimated IVR time of  $\tau_{\text{IVR}} = 3.6 \pm 0.2$  ps. The light-blue area corresponds to the standard deviation of the ensemble of trajectories. The narrow red lines show the exponential decay of the vibrational amplitude.

magnitude larger than the period of the desired chiral vibrational dynamics and should thus not obstruct observation of the chiral signal.

#### IV. NUMERICAL DETAILS OF QUANTUM-CHEMICAL CALCULATIONS

**Table S1** Equilibrium geometry of the COFCl at the B3LYP/cc-pVTZ level of theory and the geometry of the turning point for the vibrational wavepacket ( $\langle 0|\xi|1\rangle$ ). The geometries are reported in XYZ file format with coordinates are given in Ångström.

```

4
  Equilibrium structure at B3LYP/cc-pVTZ level
Cl      1.2424559624    0.0064155674    0.0000000000
C       -0.4970547972    0.1473235259    0.0000000000
F       -1.0346338274   -1.0679815724    0.0000000000
O       -1.1144924363    1.1439709190    0.0000000000

4
<0|xi|1> turning point structure
Cl      1.2424559624    0.0064155674    0.0000000000
C       -0.4970547972    0.1473235259    0.0498566330
F       -1.0346338274   -1.0679815724    0.0000000000
O       -1.1144924363    1.1439709190    0.0000000000

```

**Table S2** The ground and excited potential energy surfaces of the neutral COFCl ( $V_g$  and  $V_e$ ) and ground state potential of the COFCl cation ( $V_i$ ) along the out-of-plane vibrational coordinate  $\xi$  (see also figure S9) at the B3LYP/cc-pVTZ and TDA-B3LYP/cc-pVTZ levels of theory. The approximation is made using polynomial given in Equation 17. Coefficients  $V_n$  are given in  $\text{cm}^{-1}$ .

$n$	$V_{g,n}$	$V_{e,n}$	$V_{i,n}$
0	-5.225	50203.464	98399.653
1	0.000	0.000	0.000
2	65964.258	-217734.795	16016.701
3	0.000	0.000	0.000
4	37689.075	2212090.458	2872.946
5	0.000	0.000	0.000
6	-27411.772	-14788725.875	2005.847
7	0.000	0.000	0.000
8	-256582.066	62737810.703	-9781.540
9	0.000	0.000	0.000
10	894591.518	-154205083.960	17659.820
11	0.000	0.000	0.000
12	-1299431.830	200002541.361	-19097.394
13	0.000	0.000	0.000
14	726023.329	-105709357.157	9364.166
15	0.000	0.000	0.000

**Table S3** The ground state dipole moment dependence of the COFCI along the out-of-plane vibrational coordinate  $\xi$  at the B3LYP/cc-pVTZ level of theory. The approximation is made using polynomial given in Equation 17. Coefficients  $\mu_{g,n}^i$ ,  $i = a, b, c$  are given in debyes (D).

$n$	$\mu_{g,n}^a$	$\mu_{g,n}^b$	$\mu_{g,n}^c$
0	-0.9314524903	-0.7624595494	0.0000000000
1	0.0000000000	0.0000000000	1.9073073452
2	-0.5087896375	1.3252089900	0.0000000000
3	0.0000000000	0.0000000000	-1.0960792347
4	0.8538036739	0.3899422020	0.0000000000
5	0.0000000000	0.0000000000	0.0820464672
6	0.3526400471	-0.4585282449	0.0000000000
7	0.0000000000	0.0000000000	0.8162906684
8	-1.6358233159	1.2532774805	0.0000000000
9	0.0000000000	0.0000000000	-0.6877409655
10	2.3283039851	-2.5396816022	0.0000000000
11	0.0000000000	0.0000000000	-0.2611082534
12	-2.2711754646	2.2187633865	0.0000000000
13	0.0000000000	0.0000000000	0.6187223861
14	0.7706536394	-0.7867363304	0.0000000000
15	0.0000000000	0.0000000000	-0.2737050963

**Table S4** The ground to the first excited state transition dipole moment dependence of the COFCI along the out-of-plane vibrational coordinate  $\xi$  at the TDA-B3LYP/cc-pVTZ level of theory. The approximation is made using polynomial given in Equation 17. Coefficients  $\mu_{ge,n}^i$ ,  $i = a, b, c$  are given in debyes (D).

$n$	$\mu_{ge,n}^a$	$\mu_{ge,n}^b$	$\mu_{ge,n}^c$
0	0.0000000000	0.0000000000	0.1326949748
1	-3.3639023583	-0.5049714658	0.0000000000
2	0.0000000000	0.0000000000	-1.0422105702
3	40.7810786314	2.4622616344	0.0000000000
4	0.0000000000	0.0000000000	10.3628355130
5	-318.7583904805	-18.6065909522	0.0000000000
6	0.0000000000	0.0000000000	-54.1637848023
7	1393.0651368390	88.2305627304	0.0000000000
8	0.0000000000	0.0000000000	154.0605856734
9	-3483.7826186812	-233.5331157032	0.0000000000
10	0.0000000000	0.0000000000	-240.7596071527
11	4945.3954293408	345.2714224438	0.0000000000
12	0.0000000000	0.0000000000	194.7220465762
13	-3704.3036112783	-266.4104980060	0.0000000000
14	0.0000000000	0.0000000000	-63.7450060156
15	1136.1280526166	83.4342437049	0.0000000000



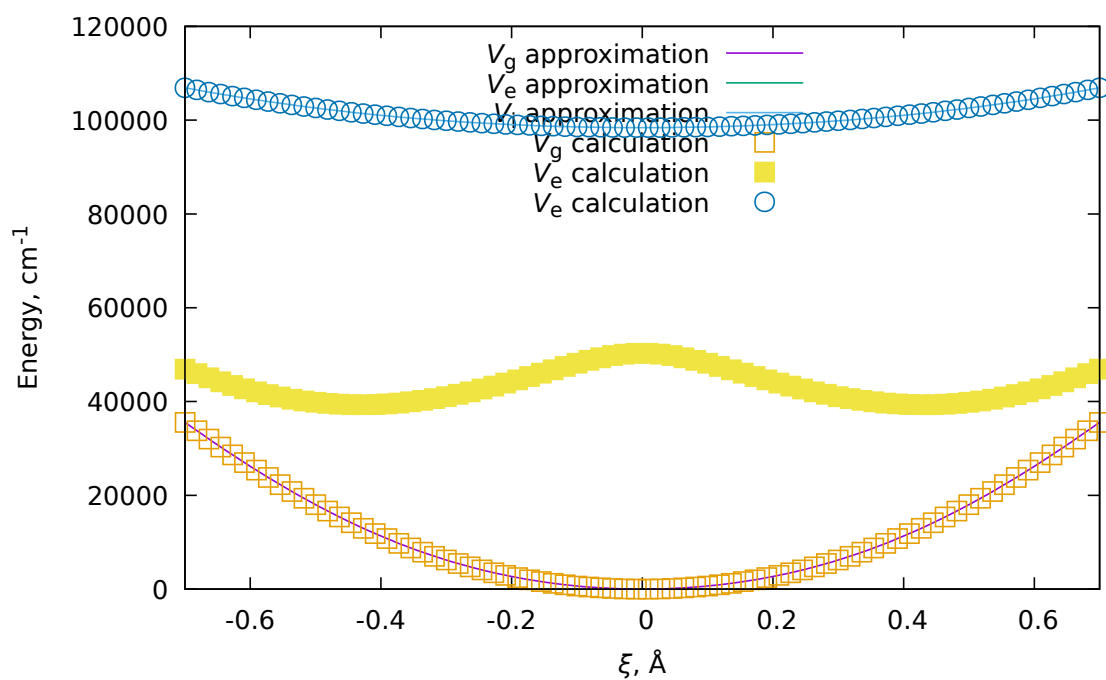


**Figure S9 Potential energy surfaces of COFCl:** Fitted ground and excited potential energy surfaces of the neutral COFCl ( $V_g(\xi)$  and  $V_e(\xi)$ ) and ground potential energy surface of the cationic COFCl ( $V_i(\xi)$ ) along the out-of-plane vibrational coordinate  $\xi$ . Points show the results of the quantum-chemical calculations, and solid lines illustrate the result of the fit.

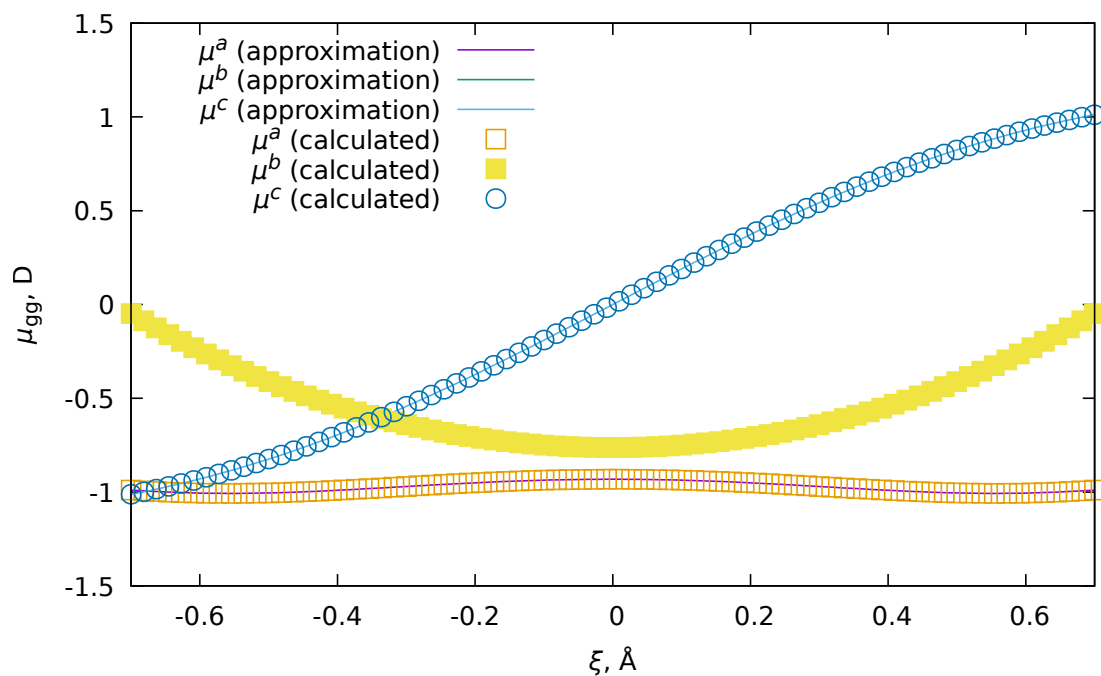


**Figure S10 Dipole moments of COFCl:** Fitted ground state dipole moments ( $\mu_g^i(\xi)$ ,  $i = a, b, c$ ) of the COFCl along the out-of-plane vibrational coordinate  $\xi$ . Points show the results of the quantum-chemical calculations, and solid lines illustrate the result of the fit.

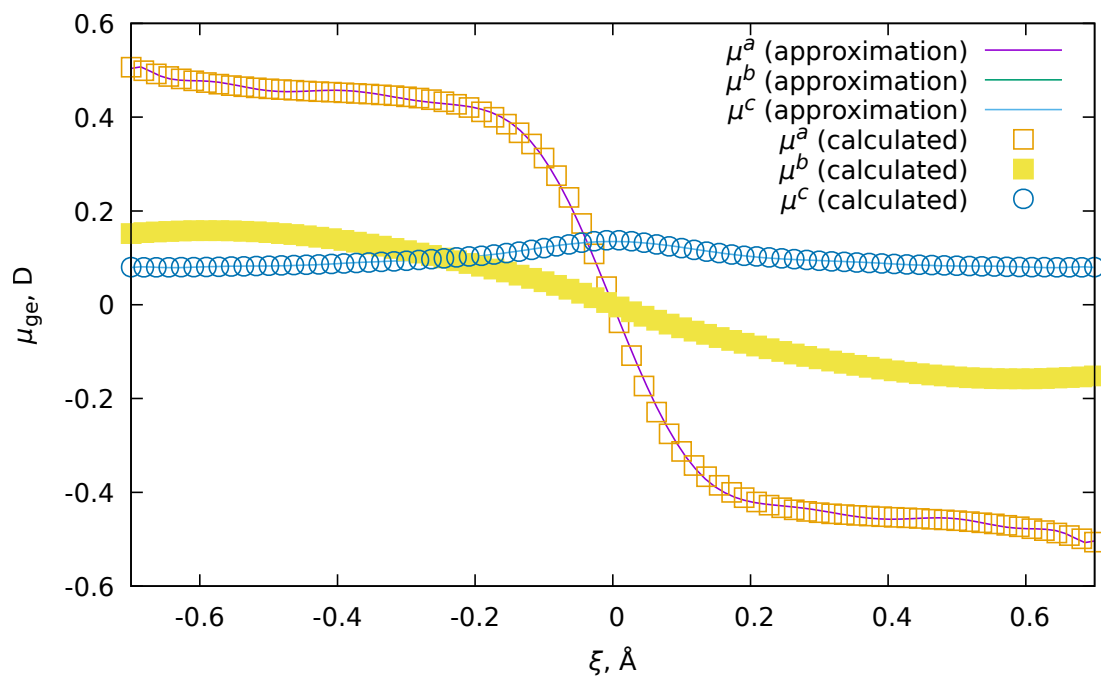


**Figure S11 Transition dipole moments:** Fitted ground to excited state transition dipole moments ( $\mu_{\text{g}}^i(\xi)$ ,  $i = a, b, c$ ) of the COFCI along the out-of-plane vibrational coordinate  $\xi$ . Points show the results of the quantum-chemical calculations, and solid lines illustrate the result of the fit.

## V. CALCULATION OF THE CLASSICAL SELECTION RULES USING wxMAXIMA

Here, we provide the code in wxMaxima that was used to evaluate the selection rules for the enantiomeric signal, given in section IB.

```
R1(phi):= matrix([cos(phi), -sin(phi), 0],
                [sin(phi),  cos(phi), 0],
                [ 0      ,   0,      1]);
R2(theta):= matrix([1, 0, 0],
                  [0, cos(theta), -sin(theta)],
                  [0, sin(theta),  cos(theta)]);
R3(chi) :=matrix([cos(chi), -sin(chi), 0],
                 [sin(chi),  cos(chi), 0],
                 [ 0      ,   0,      1]);
R(phi,theta,chi) := ((R3(chi)).R2(theta)).(R1(phi));
J(theta):= sin(theta);

a1 : matrix([a1x,a1y,a1z]);
a2 : matrix([a2x,a2y,a2z]);
a3 : matrix([a3x,a3y,a3z]);
mu1 : matrix([m1x, m1y, m1z]);
mu2 : matrix([m2x, m2y, m2z]);
mu3 : matrix([m3x, m3y, m3z]);

Q1(phi,theta,chi):= (mu1.R(phi,theta,chi).a1);
integrate( integrate( integrate(Q1(phi,theta,chi)*J(theta), phi, 0, 2*%pi ),
                             theta, 0, %pi ) , chi, 0 , 2*%pi );

Q2(phi,theta,chi):= Q1(phi,theta,chi)*(mu2.R(phi,theta,chi).a2);
integrate( integrate( integrate(Q2(phi,theta,chi)*J(theta), phi, 0, 2*%pi ),
                             theta, 0, %pi ) , chi, 0 , 2*%pi );

Q3(phi,theta,chi):= Q2(phi,theta,chi)*(mu3.R(phi,theta,chi).a3);
integrate( integrate( integrate(Q3(phi,theta,chi)*J(theta), phi, 0, 2*%pi ),
                             theta, 0, %pi ) , chi, 0 , 2*%pi );
```

## VI. CALCULATION OF THE TRANSITION DIPOLE MOMENTS FROM THE ONE-DIMENSIONAL SCHRÖDINGER EQUATION

Here, we provide the Python code that was used for solving the one-dimensional Schrödinger equation to obtain the vibronic energy levels, the permanent dipole moments, and the transition dipole moments.

```
1 import numpy as np
2 import sys
3 import argparse
4 import scipy.interpolate as spi
5 from copy import deepcopy
6 import scipy.linalg as spla
7
8 KinEnCoeff=33.7152313
9
10 def sincD1(i,j):
11     if i==j:
12         return 0.0
13     else:
14         return (-1.0)**(i-j)/(i-j)
15
16 def sincD2(i,j):
17     if i==j:
18         return -(np.pi**2)/3.0
```

```

19     else:
20         return -2.0*(-1.0)**(i-j)/(i-j)**2
21
22
23 def KinEnergy(X,M):
24     #G = 0.5*KinEnCoeff/M
25
26     Nmat = len(X)
27     dx = np.average(X[1:] - X[:-1])
28
29     D2 = np.array([[sincD2(i,j) for j in range(0,Nmat)] for i in range(0,Nmat)])/(dx**2)
30
31     print(" dx = %15.10f Angstrom" % dx)
32
33     Res = -D2*0.5*KinEnCoeff/M
34
35     print(" Deviation from Hermitivity in T = %15.10f" % (np.max(np.abs( Res.flatten() - Res.T.
36     flatten() ))) )
37     return Res
38
39 def PotEnergy(V, Vmin=None):
40     if Vmin is None:
41         vmin = min(V)
42     else:
43         vmin=Vmin
44     return np.diag(V-vmin)
45 #####
46
47 parser = argparse.ArgumentParser()
48 parser.add_argument("-f", "--filename", help="input file name", type=str, default="ini.dat")
49 parser.add_argument("-m", "--mass", help="reduced mass of the vibration in a.m.u.", type=float,
50     default=1.0)
51 parser.add_argument("--IniState", help="Initial state (>=0)", type=int, default=0)
52 parser.add_argument("--FinState", help="Final State Number (>=0)", type=int, default=1)
53 parser.add_argument("--NGS2P", help="Number of ground states to print", type=int, default=5)
54 parser.add_argument("--NES2P", help="Number of excited states to print", type=int, default=None)
55 parser.add_argument("-n", "--NumOfPts", help="Size of the Hamiltonian matrix", type=int, default
56     =800)
57 parser.add_argument("--InterpolType", help="interpolation type", type=str, choices=['linear', '
58     quadratic', 'cubic'], default='cubic')
59 parser.add_argument('--SymmExc', action='store_true', help="Flag to symmetrize the excited state."
60     )
61 parser.add_argument('--PrintPolTensors', action='store_true', help="Flag to print the
62     polarizability tensors.")
63
64
65 args = parser.parse_args()
66
67 #####
68 print(" File to process: "+args.filename)
69 data = np.loadtxt(args.filename)
70
71 X0 = data[:,0]
72 Vgr = spi.interp1d(X0,data[:,1], kind=args.InterpolType)
73 Vex = spi.interp1d(X0,data[:,2], kind=args.InterpolType)
74
75
76 x = np.linspace(np.min(X0),np.max(X0),args.NumOfPts)
77
78
79 ### Solve ground state problem
80 vg = Vgr(x)
81 ve = Vex(x)
82
83 Vmin = min(vg)
84
85 H = KinEnergy(x, args.mass) + PotEnergy(vg, Vmin=Vmin)

```

```

83 Eg,WFNg = np.linalg.eigh(H)
84
85 for n in range(0,len(Eg)):
86     WFNg[:,n]/=np.sqrt(np.dot(WFNg[:,n],WFNg[:,n]))
87
88
89 print("Ground electronic state vibrational levels:\n")
90 for n in range(0,args.NGS2P):
91     print(" %3i  %15.10f %15.10f " % (n, Eg[n], Eg[n]-Eg[0]) )
92
93 np.savetxt("dump0.wfn", np.stack([x] + [w for w in WFNg.T[0:args.NGS2P] ], axis=-1) )
94
95 Vmin = min(ve)
96 H = KinEnergy(x, args.mass) + PotEnergy(ve, Vmin=Vmin)
97
98 Ee,WFNe = np.linalg.eigh(H)
99
100 if args.SymmExc:
101     print("Started symmetrization in the excited states, %i states in total" % len(Ee) )
102
103     def symmWfn(wfn, Coeff=1.0):
104         res = wfn + Coeff * np.flip(wfn)
105         res /= np.sqrt(np.dot(res, res))
106         return res
107
108     # symmetric representation
109     sWFNe = np.array([ symmWfn(wfn, Coeff=1.0) for wfn in WFNe.T ])
110
111     rank = np.linalg.matrix_rank(sWFNe)
112     print("Symmetric WFNs : %i" % rank)
113
114     mask = True + np.zeros(sWFNe.shape[0], dtype=bool)
115     print(mask[mask].shape)
116     for i in range(1,sWFNe.shape[0]):
117         for j in range(0,i):
118             if np.abs(np.dot(sWFNe[i],sWFNe[j]))>0.5 and mask[j]:
119                 mask[i] = False
120     print(mask[mask].shape)
121     sWFNe = sWFNe[mask]
122     np.savetxt("symmetric.wfn", np.concatenate([[x],sWFNe]).T )
123
124     sEe = np.array([np.dot(wfn,np.dot(H,wfn)) for wfn in sWFNe])
125
126     # antisymmetric representation
127     aWFNe = np.array([ symmWfn(wfn, Coeff=-1.0) for wfn in WFNe.T ])
128
129     rank = np.linalg.matrix_rank(aWFNe)
130     print("Antisymmetric WFNs : %i" % rank)
131
132     mask = True + np.zeros(aWFNe.shape[0], dtype=bool)
133     for i in range(1,aWFNe.shape[0]):
134         for j in range(0,i):
135             if np.abs(np.dot(aWFNe[i],aWFNe[j]))>0.5 and mask[j]:
136                 mask[i] = False
137     print(mask[mask].shape)
138     aWFNe = aWFNe[mask]
139     np.savetxt("antisymmetric.wfn", np.concatenate([[x],aWFNe]).T )
140
141     aEe = np.array([np.dot(wfn,np.dot(H,wfn)) for wfn in aWFNe])
142
143     WFNe = np.concatenate([sWFNe,aWFNe])
144     Ee = np.concatenate([sEe,aEe])
145     print(WFNe.shape,Ee.shape)
146
147     inds = np.argsort(Ee)
148
149     WFNe = WFNe[inds].T
150     Ee = Ee[inds]
151     print(WFNe.shape,Ee.shape)
152

```

```

153
154 if args.NES2P is None:
155     args.NES2P = len(Ee)
156
157
158 Ee += min(ve) - min(vg)
159
160
161 for n in range(0, len(Ee)):
162     WFNe[:, n] /= np.sqrt(np.dot(WFNe[:, n], WFNe[:, n]))
163
164
165 print("Excited electronic state vibrational levels:\n")
166 for n in range(0, args.NES2P):
167     print(" %3i %15.10f %15.10f %15.10f" % (n, Ee[n], Ee[n]-Ee[0], Ee[n]-Eg[0]) )
168
169 np.savetxt("dump1.wfn", np.stack([x] + [w for w in WFNe.T[0:args.NES2P] ], axis=-1) )
170
171 TrD=None
172 if len(data[0]) >=6:
173     TrD=[]
174     TrD.append(spi.interp1d(X0, data[:, 3], kind=args.InterpolType)(x) )
175     TrD.append(spi.interp1d(X0, data[:, 4], kind=args.InterpolType)(x) )
176     TrD.append(spi.interp1d(X0, data[:, 5], kind=args.InterpolType)(x) )
177
178
179 D0=None
180 if len(data[0]) >=9:
181     D0=[]
182     D0.append(spi.interp1d(X0, data[:, 6], kind=args.InterpolType)(x) )
183     D0.append(spi.interp1d(X0, data[:, 7], kind=args.InterpolType)(x) )
184     D0.append(spi.interp1d(X0, data[:, 8], kind=args.InterpolType)(x) )
185
186
187 np.set_printoptions(suppress=True, precision=12)
188
189
190 outf = open("raman_and_static.res", "w")
191 outf1 = open("absorbtion.sp", "w")
192
193 if args.PrintPolTensors:
194     outf2 = open("pol_tensors.dat", "w")
195
196
197 d00 = np.array([np.dot(WFNg[:, args.IniState], D0[i]*WFNg[:, args.IniState]) for i in range(0,3) ])
198 print(d00)
199
200
201 for n, vState in enumerate(WFNe.T):
202
203     E0v = Ee[n]-Eg[args.IniState]
204     Ev1 = Ee[n]-Eg[args.FinState]
205
206     d0n = np.array([np.dot(vState, TrD[i]*WFNg[:, args.IniState]) for i in range(0,3) ])
207     dn1 = np.array([np.dot(vState, TrD[i]*WFNg[:, args.FinState]) for i in range(0,3) ])
208
209
210     dV = np.dot(d00, np.cross(d0n, dn1))
211     outf.write(" %15.2f %15.2f %15.10f " % (E0v, Ev1, dV) )
212     outf.write("\n")
213
214     outf1.write(" %15.3f %15.3f %15.10f \n" % (E0v, 1.0e7/E0v, np.dot(d0n, d0n)) )
215
216     if args.PrintPolTensors:
217         outf2.write("\n\n |%i, g> -> |%i, e> -> |%i, g> : \n" % (args.IniState, n, args.FinState) )
218         pt = np.outer(d0n, dn1)
219         outf2.write(str(pt)+"\n\n")
220
221 D2S = [x, vg, ve]
222 if not TrD is None:

```



```
223     D2S = D2S + TrD
224 if not D0 is None:
225     D2S = D2S + D0
226
227 np.savetxt("extrapolated_values.dat", np.stack(D2S ,axis=-1))
```

## REFERENCES AND NOTES

1. D. P. Glavin, A. S. Burton, J. E. Elsila, J. C. Aponte, J. P. Dworkin, The search for chiral asymmetry as a potential biosignature in our solar system. *Chem. Rev.* **120**, 4660–4689 (2020).
2. M. Quack, J. Stohner, M. Willeke, High-resolution spectroscopic studies and theory of parity violation in chiral molecules. *Annu. Rev. Phys. Chem.* **59**, 741–769 (2008).
3. U. Raucci, H. Weir, C. Bannwarth, D. M. Sanchez, T. J. Martínez, Chiral photochemistry of achiral molecules. *Nat. Commun.* **13**, 2091 (2022).
4. C. Fábri, L. Horný, M. Quack, Tunneling and parity violation in trisulfane (HSSSH): An almost ideal molecule for detecting parity violation in chiral molecules. *ChemPhysChem* **16**, 3584–3589 (2015).
5. Y. Fujimura, L. González, K. Hoki, J. Manz, Y. Ohtsuki, Selective preparation of enantiomers by laser pulses: Quantum model simulation for H<sub>2</sub>POSH. *Chem. Phys. Lett.* **306**, 1–8 (1999).
6. D. Gerbasi, P. Brumer, I. Thanopoulos, P. Král, M. Shapiro, Theory of the two step enantiomeric purification of 1,3 dimethylallene. *J. Chem. Phys.* **120**, 11557–11563 (2004).
7. E. F. Thomas, N. E. Henriksen, Phase-modulated nonresonant laser pulses can selectively convert enantiomers in a racemic mixture. *J. Phys. Chem. Lett.* **8**, 2212–2219 (2017).
8. M. Quack, G. Seyfang, G. Wichmann, Fundamental and approximate symmetries, parity violation and tunneling in chiral and achiral molecules. *Adv. Quantum Chem.* **81**, 51–104 (2020).
9. A. F. Ordonez, O. Smirnova, Generalized perspective on chiral measurements without magnetic interactions. *Phys. Rev. A* **98**, 063428 (2018).
10. B. Ritchie, Theory of the angular distribution of photoelectrons ejected from optically active molecules and molecular negative ions. *Phys. Rev. A* **13**, 1411–1415 (1976).
11. N. Böwering, T. Lischke, B. Schmidtke, N. Müller, T. Khalil, U. Heinzmann, Asymmetry in photoelectron emission from chiral molecules induced by circularly polarized light. *Phys. Rev. Lett.* **86**, 1187–1190 (2001).
12. C. Lux, M. Wollenhaupt, T. Bolze, Q. Liang, J. Köhler, C. Sarpe, T. Baumert, Circular dichroism in the photoelectron angular distributions of camphor and fenchone from multiphoton ionization with femtosecond laser pulses. *Angew. Chem. Int. Ed.* **51**, 5001–5005 (2012).
13. A. Comby, S. Beaulieu, M. Boggio-Pasqua, D. Descamps, F. Légaré, L. Nahon, S. Petit, B. Pons, B. Fabre, Y. Mairesse, V. Blanchet, Relaxation dynamics in photoexcited chiral molecules studied by

- time-resolved photoelectron circular dichroism: Toward chiral femtochemistry. *J. Phys. Chem. Lett.* **7**, 4514–4519 (2016).
14. S. Beaulieu, A. Comby, A. Clergerie, J. Caillat, D. Descamps, N. Dudovich, B. Fabre, R. Géneaux, F. Légaré, S. Petit, B. Pons, G. Porat, T. Ruchon, R. Taïeb, V. Blanchet, Y. Mairesse, Attosecond-resolved photoionization of chiral molecules. *Science* **358**, 1288–1294 (2017).
  15. V. Svoboda, N. B. Ram, D. Baykusheva, D. Zindel, M. D. J. Waters, B. Spenger, M. Ochsner, H. Herburger, J. Stohner, H. J. Wörner, Femtosecond photoelectron circular dichroism of chemical reactions. arXiv:2206.04099 [physics.chem-ph] (8 June 2022).
  16. K. Fehre, S. Eckart, M. Kunitski, M. Pitzer, S. Zeller, C. Janke, D. Trabert, J. Rist, M. Weller, A. Hartung, L. P. H. Schmidt, T. Jahnke, R. Berger, R. Dörner, M. S. Schöffler, Enantioselective fragmentation of an achiral molecule in a strong laser field. *Sci. Adv.* **5**, eaau7923 (2019).
  17. D. Baykusheva, D. Zindel, V. Svoboda, E. Bommeli, M. Ochsner, A. Tehlar, H. J. Wörner, Real-time probing of chirality during a chemical reaction. *Proc. Natl. Acad. Sci. U.S.A.* **116**, 23923–23929 (2019).
  18. S. S. Bychkov, B. A. Grishanin, V. N. Zadkov, H. Takahashi, Laser coherent control of molecular chiral states via entanglement of the rotational and torsional degrees of freedom. *J. Raman Spectrosc.* **33**, 962–973 (2002).
  19. D. V. Zhdanov, V. N. Zadkov, Coherent control of chirality in ensemble of randomly oriented molecules using a sequence of short laser pulses. *Laser Physics* **20**, 107–118 (2010).
  20. A. F. Ordonez, O. Smirnova, Propensity rules in photoelectron circular dichroism in chiral molecules. I. Chiral hydrogen. *Phys. Rev. A* **99**, 043416 (2019).
  21. C. P. Koch, M. Lemeshko, D. Sugny, Quantum control of molecular rotation. *Rev. Mod. Phys.* **91**, 035005 (2019).
  22. D. L. Andrews, T. Thirunamachandran, On three-dimensional rotational averages. *J. Chem. Phys.* **67**, 5026–5033 (1977).
  23. M. Leibscher, T. F. Giesen, C. P. Koch, Principles of enantio-selective excitation in three-wave mixing spectroscopy of chiral molecules. *J. Chem. Phys.* **151**, 014302 (2019).
  24. I. Powis, in *Photoelectron Circular Dichroism in Chiral Molecules*, S. A. Rice, Ed. (John Wiley & Sons Ltd., 2008), chap. 5, pp. 267–329.
  25. M. H. M. Janssen, I. Powis, Detecting chirality in molecules by imaging photoelectron circular dichroism. *Phys. Chem. Chem. Phys.* **16**, 856–871 (2014).

26. C. Lux, M. Wollenhaupt, C. Sarpe, T. Baumert, Photoelectron circular dichroism of bicyclic ketones from multiphoton ionization with femtosecond laser pulses. *ChemPhysChem* **16**, 115–137 (2015).
27. A. Kastner, C. Lux, T. Ring, S. Züllighoven, C. Sarpe, A. Senftleben, T. Baumert, Enantiomeric excess sensitivity to below one percent by using femtosecond photoelectron circular dichroism. *ChemPhysChem* **17**, 1119–1122 (2016).
28. G. Meijer, in *Molecular Beams in Physics and Chemistry: From Otto Stern's Pioneering Exploits to Present-Day Feats*, B. Friedrich, H. Schmidt-Böcking, Eds. (Springer International Publishing, 2021), pp. 463–476.
29. R. E. Goetz, C. P. Koch, L. Greenman, Quantum control of photoelectron circular dichroism. *Phys. Rev. Lett.* **122**, 013204 (2019).
30. R. E. Goetz, C. P. Koch, L. Greenman, Perfect control of photoelectron anisotropy for randomly oriented ensembles of molecules by XUV REMPI and polarization shaping. *J. Chem. Phys.* **151**, 074106 (2019).
31. E. Ruch, Chiral derivatives of achiral molecules: Standard classes and the problem of a right-left classification. *Angew. Chem. Int. Ed.* **16**, 65–72 (1977).
32. G. Hartmann, M. Ilchen, P. Schmidt, C. Küstner-Wetekam, C. Ozga, F. Scholz, J. Buck, F. Trinter, J. Viefhaus, A. Ehresmann, M. S. Schöffler, A. Knie, P. V. Demekhin, Recovery of high-energy photoelectron circular dichroism through fano interference. *Phys. Rev. Lett.* **123**, 043202 (2019).
33. B. Friedrich, D. Herschbach, Enhanced orientation of polar molecules by combined electrostatic and nonresonant induced dipole forces. *J. Chem. Phys.* **111**, 6157–6160 (1999).
34. S. V. Krasnoshchekov, V. B. Laptev, S. A. Klimin, I. K. Gainullin, A. A. Makarov, Overtone spectroscopy of  $\nu(\text{C}=\text{O})$  stretching vibration of hexafluoroacetone: Experimental and ab initio determination of peak positions, absolute intensities, and band shapes. *Spectrochim. Acta A Mol. Biomol. Spectrosc.* **238**, 118396 (2020).
35. S. Takeda, R. Tarao, The infrared spectra of alkylaluminum-ether complexes. *Bull. Chem. Soc. Jpn.* **38**, 1567–1574 (1965).
36. H. Hoberg, S. Krause, The Al—Al bond as a readily accessible structural unit in organometallic compounds. *Angew. Chem. Int. Ed.* **15**, 694–694 (1976).
37. A. Kunicki, W. Kosińska, M. Bolesławski, S. Pasynkiewicz, The  $^1\text{H}$  NMR spectra of methylmethoxyaluminium chloride and methylmethoxyaluminium iodide. *J. Organomet. Chem.* **141**, 283–288 (1977).

38. A. D. Becke, Density-functional thermochemistry. III. The role of exact exchange. *J. Chem. Phys.* **98**, 5648–5652 (1993).
39. C. Lee, W. Yang, R. G. Parr, Development of the Colle-Salvetti correlation-energy formula into a functional of the electron density. *Phys. Rev. B* **37**, 785–789 (1988).
40. S. H. Vosko, L. Wilk, M. Nusair, Accurate spin-dependent electron liquid correlation energies for local spin density calculations: A critical analysis. *Can. J. Phys.* **59**, 1200–1211 (1980).
41. P. J. Stephens, F. J. Devlin, C. F. Chabalowski, M. J. Frisch, Ab initio calculation of vibrational absorption and circular dichroism spectra using density functional force fields. *J. Phys. Chem.* **98**, 11623–11627 (1994).
42. T. H. Dunning Jr., Gaussian basis sets for use in correlated molecular calculations. i. The atoms boron through neon and hydrogen. *J. Chem. Phys.* **90**, 1007–1023 (1989).
43. S. Hirata, M. Head-Gordon, Time-dependent density functional theory within the Tamm-Dancoff approximation. *Chem. Phys. Lett.* **314**, 291–299 (1999).
44. F. Neese, The ORCA program system. *Wiley Interdiscip. Rev. Comput. Mol. Sci.* **2**, 73–78 (2012).
45. D. T. Colbert, W. H. Miller, A novel discrete variable representation for quantum mechanical reactive scattering via the *S*-matrix Kohn method. *J. Chem. Phys.* **96**, 1982–1991 (1992).
46. I. Zanon, G. Giacometti, D. Picciol, The electronic spectrum of FCICO. *Spectrochim. Acta A Mol. Biomol. Spectrosc.* **19**, 301-E7 (1963).
47. N. Heineking, W. Jager, M. Gerry, Isotopic and vibrational satellites in the rotational spectrum of carbonyl chloride fluoride. *J. Mol. Spectrosc.* **158**, 69–81 (1993).
48. C. Maul, C. Dietrich, T. Haas, K.-H. Gericke, Photodissociation dynamics of carbonyl chloride fluoride and its implications for phosgene three body decay. *Phys. Chem. Chem. Phys.* **1**, 1441–1446 (1999).
49. A. Perrin, J. Demaison, G. Toon, The  $\nu_1$ ,  $\nu_2$ , and  $\nu_3$  bands of carbonyl chlorofluoride (COFCl) at 5.3, 9.1, and 13.1  $\mu\text{m}$ : Position and intensity parameters and their use for atmospheric studies. *J. Quant. Spectrosc. Radiat. Transf.* **112**, 1266–1279 (2011).
50. H. Keller-Rudek, G. K. Moortgat, R. Sander, R. Sørensen, The MPI-Mainz UV/VIS spectral atlas of gaseous molecules of atmospheric interest. *Earth Syst. Sci. Data* **5**, 365–373 (2013).
51. H.-J. Werner, P. J. Knowles, G. Knizia, F. R. Manby, M. Schütz, P. Celani, T. Korona, R. Lindh, A. Mitrushenkov, G. Rauhut, K. R. Shamasundar, T. B. Adler, R. D. Amos, A. Bernhardsson, A. Berning, D. L. Cooper, M. J. O. Deegan, A. J. Dobbyn, F. Eckert, E. Goll, C. H. I, A. Hesselmann, G.

- Hetzer, T. Hrenar, G. Jansen, C. Köppl, Y. Liu, A. W. Lloyd, R. A. Mata, A. J. May, S. J. McNicholas, W. Meyer, M. E. Mura, A. Nicklass, D. P. O'Neill, P. Palmieri, D. Peng, K. Pflüger, R. Pitzer, M. Reiher, T. Shiozaki, H. Stoll, A. J. Stone, R. Tarroni, T. Thorsteinsson, M. Wang, MOLPRO, version 2012.1, a package of ab initio programs.
52. H.-J. Werner, P. J. Knowles, G. Knizia, F. R. Manby, M. Schütz, Molpro: A general-purpose quantum chemistry program package. *Wiley Interdiscip. Rev. Comput. Mol. Sci.* **2**, 242–253 (2012).
53. R. A. Kendall, T. H. Dunning Jr., R. J. Harrison, Electron affinities of the first-row atoms revisited. Systematic basis sets and wave functions. *J. Comp. Phys.* **96**, 6796–6806 (1992).
54. F. A. Gianturco, R. R. Lucchese, N. Sanna, Calculation of low-energy elastic cross sections for electron-CF<sub>4</sub> scattering. *J. Chem. Phys.* **100**, 6464–6471 (1994).
55. A. P. P. Natalense, R. R. Lucchese, Cross section and asymmetry parameter calculation for sulfur 1s photoionization of SF<sub>6</sub>. *J. Chem. Phys.* **111**, 5344–5348 (1999).
56. P. Hockett, M. Wollenhaupt, C. Lux, T. Baumert, Complete photoionization experiments via ultrafast coherent control with polarization multiplexing. II. Numerics and analysis methodologies. *Phys. Rev. A* **92**, 013411 (2015).
57. S. Grimme, S. Ehrlich, L. Goerigk, Effect of the damping function in dispersion corrected density functional theory. *J. Comput. Chem.* **32**, 1456–1465 (2011).
58. F. Weigend, R. Ahlrichs, Balanced basis sets of split valence, triple zeta valence and quadruple zeta valence quality for h to rn: Design and assessment of accuracy. *Phys. Chem. Chem. Phys.* **7**, 3297–3305 (2005).
59. P. Atkins, J. Paula, *Atkins' Physical Chemistry* (Oxford Univ. Press, 2008).
60. M. Mantina, A. C. Chamberlin, R. Valero, C. J. Cramer, D. G. Truhlar, Consistent van der Waals radii for the whole main group. *Chem. A Eur. J.* **113**, 5806–5812 (2009).